J. Mech. Phys. Solids 169 (2022) 105084

Contents lists available at ScienceDirect

Journal of the Mechanics and Physics of Solids

journal homepage: www.elsevier.com/locate/jmps

Buckling of viscoelastic spherical shells

Tianzhen Liu [a], Yuzhen Chen [b], John W. Hutchinson [c], Lihua Jin [b,*]

[a] Key Laboratory of C & PC Structures of Ministry of Education, National Prestress Engineering Research Center, Southeast University, Nanjing 210096, China
[b] Department of Mechanical and Aerospace Engineering, University of California, Engineering Building IV 37-134, 420, Los Angeles, CA 90095, USA
[c] School of Engineering and Applied Sciences, Harvard University, Cambridge, MA 02138, USA

ARTICLE INFO

Keywords:
Spherical shells
Viscoelasticity
Creep buckling
Imperfection
Shell theory

ABSTRACT

Viscoelastic spherical shells exhibit a wide range of time/rate-dependent buckling behaviors when subjected to pressure. For certain loadings, buckling can even occur after a significant time delay, termed creep buckling. To gain a thorough understanding of the nonlinear time-dependent buckling behavior of viscoelastic spherical shells, this work develops an analytical model employing the small-strain, moderate-rotation shell theory combined with a linearly viscoelastic material law. Numerical results are presented for axisymmetric spherical shells with geometric imperfections for two types of loading: a prescribed rate of volume change and a prescribed pressure that remains constant after it is applied. The first type reveals the rate-dependent behavior of viscoelastic buckling while the constant pressure loading is used to quantify creep buckling phenomena. The results show that viscoelasticity and loading rates play important roles in the load-carrying behavior of these shells, and the results for the constant pressure loading reveal an unexpected and important connection between the short-time elastic buckling limit and the long-time creep buckling limit. An imperfection sensitivity map is constructed for the constant pressure loading showing three regimes with qualitatively different behaviors: near-instantaneous buckling, creep buckling and no buckling.

1. Introduction

Spherical shells, serving as essential and indispensable structures and structural components, exhibit diverse functionalities (Bartlett et al., 2015; Cheng et al., 2021; Faber et al., 2020; Gorissen et al., 2020; Qiao et al., 2021; Vasios et al., 2021; Yang et al., 2021) and have widespread utilization in various engineering fields (Błachut and Magnucki, 2008; Jose et al., 2014). The buckling behavior of spherical shells has drawn considerable research attention (Audoly and Hutchinson, 2019; Budiansky, 1974; Dong et al., 2020; Huang, 1963; Huang, 1964; Hutchinson and Koiter, 1970; Karman and Tsien, 1939; Koiter, 1969; Paulose and Nelson, 2013; Qiao et al., 2020), due to the ubiquitous importance of these structures and the fact that buckling can result in their catastrophic collapse. On the other hand, shell buckling offers new opportunities for functional designs of structures as demand by virtue of its nonlinear behavior (Bartlett et al., 2015; Chen et al., 2022; Faber et al., 2020; Kochmann and Bertoldi, 2017; Qiao et al., 2021; Reis, 2015).

Shell theories have been developed to quantitatively predict the critical buckling loads for shells with linearly elastic material behavior (Huang, 1964; Hutchinson, 2016; Hutchinson and Thompson, 2017; Karman and Tsien, 1939; Koga and Hoff, 1969; Koiter, 1969; Krenzke and Kiernan, 1963). Decades of research has shown that there are significant discrepancies between theoretically

* Corresponding author.
E-mail address: lihuajin@seas.ucla.edu (L. Jin).

https://doi.org/10.1016/j.jmps.2022.105084
Received 14 June 2022; Received in revised form 20 September 2022; Accepted 22 September 2022
Available online 3 October 2022

predicted buckling loads and experimental observations for spherical shells loaded by external pressure, which is attributed to high imperfection sensitivity of shells (Carlson et al., 1967; Hutchinson and Thompson, 2018; Kaplan and Fung, 1954; Karman and Tsien, 1939; Koga and Hoff, 1969; Koiter, 1969). Recently, leveraging a rapid prototyping technique to fabricate elastomeric spherical shells with precisely engineered imperfections, researchers have demonstrated that shell theories can nevertheless accurately predict the buckling behavior as long as imperfections of accurate geometry are appropriately introduced into the theories (Dong et al., 2020; Hutchinson, 2016; Lee et al., 2016; Qiao et al., 2020).

Although the rich buckling behavior of shells with linearly elastic material behavior has been extensively investigated, shells made from viscoelastic materials, on the other hand, can introduce additional novel features to shell buckling behavior due to their inherent time-dependent and rate-dependent properties (Brinkmeyer et al., 2012; Che et al., 2019; Dykstra et al., 2019; Janbaz et al., 2020; Lakes, 1998; Liu et al., 2021). In particular, the phenomenon of creep buckling, i.e. buckling of a viscoelastic shell after a certain delayed period of loading when the shell is subjected to a load lower than its instantaneous buckling load, can occur (Hayman, 1981; Minahen and Knauss, 1993; Miyazaki and Hagihara, 2015). Buckling of viscoelastic shells has previously been investigated for metallic and composite shells at high temperatures (Kao, 1981; Marques and Creus, 1994; Miyazaki and Hagihara, 2015; Wilson and Vinson, 1984). The recent trend of building soft robots, architected materials and metamaterials from viscoelastic elastomers motivated the following studies of viscoelastic shells (Bartlett et al., 2015; Che et al., 2019; Chen et al., 2022; Dykstra et al., 2019; Faber et al., 2020; Janbaz et al., 2020).

Buckling of viscoelastic beams and plates has been broadly studied (Hayman, 1981; Kempner, 1954; Nachbar and Huang, 1967; Vinogradov, 1987). Creep buckling is analyzed in viscoelastic columns (Vinogradov, 1987), shallow Mises trusses (Huang, 1967), shallow arches (Huang, 1967), and other simple structural models (Hayman, 1981). The critical buckling time and load, and the post-buckling deflection, have been determined (Huang, 1967). Comparing the analytical prediction with the experimental measured creep buckling condition of viscoelastic polymeric columns, Minahen and Knauss (1993) showed that analytical modeling can predict the short-term and slow growth phases of the responses reasonably well. Buckling analysis was also conducted for viscoelastic plates to demonstrate their time-dependent buckling behavior (Hewitt and Mazumdar, 1977; Wilson and Vinson, 1984). The results show that viscoelasticity can cause a significant decrease in buckling resistance (Wilson and Vinson, 1984) when the loads are applied for sufficiently long periods of time.

Although the role of viscoelasticity on buckling of beams and plates, which tend to buckle in a stable manner, has been established, an understanding of the buckling behavior of viscoelastic shells, especially deep shells, which have the potential to buckle catastrophically, remains to be revealed with more clarity. In early work by Huang (1965), the governing equations of viscoelastic shallow shells were established by applying the corresponding principle of an elastic case with the material property evolving as a function of time, from which the critical time for buckling was evaluated numerically. Obrecht (1977) formulated an incremental viscoelastic shell theory for cylindrical shells under axial compression. The axisymmetric and/or non-axisymmetric buckling conditions were determined for spherical shells and circular cylindrical shells by a perturbation method (Grigoliuk and Lipovtsev, 1969; Jones, 1976; Obrecht, 1977; Vinogradov and Glockner, 1980; Xirouchakis and Jones, 1980), or the finite element method (Miyazaki et al., 1977). Imperfections were shown to have a significant impact on shortening the creep buckling time (Kao, 1981). Recently, the creep buckling behavior of shell structures, including both cylindrical shells and spherical shells, was reviewed, and creep buckling criteria were summarized (Miyazaki and Hagihara, 2015). However, buckling analysis of viscoelastic shells, especially spherical shells, is largely based on the shallow shell assumption. Relevant specifically to the present investigation is the study of viscoelastic spherical shells made of a silicone elastomer (Stein-Montalvo et al., 2021), where creep buckling of these shells is demonstrated experimentally and modelled by simply treating the creep deformation as an evolving defect. Thus, there is ample opportunity to explore the effect of viscoelasticity on the rate-dependent buckling and creep buckling of imperfection sensitive shells – this paper represents a step in that direction.

The present paper employs a shell theory capable of describing the deformation and buckling of deep viscoelastic spherical shells subjected to external pressure. The small-strain, moderate-rotation shell theory, combined with the standard linear viscoelastic solid for the shell material, is used. Imperfection sensitivity of elastic shells (viscoelastic shells evaluated under rapid loading) is first analyzed, revealing the knockdown of the buckling pressure due to geometric imperfections. Then, material viscoelasticity and loading rates are shown to have appreciable effects on buckling. Distinctly different behaviors are quantified, including near-instantaneous elastic buckling, creep buckling with time delays, and no buckling. An imperfection sensitivity map of these distinct responses is constructed.

The paper is organized as follows. In Section 2, the small-strain, moderate-rotation shell theory and the viscoelastic material law are combined to formulate the viscoelastic shell theory. The equilibrium equations are developed using the principle of virtual work. In Section 3, the imperfection sensitivity and the rate-dependent buckling behavior of viscoelastic shells are illustrated for two types of loading: a prescribed constant rate of volume change and a prescribed step loading of external pressure. In Section 4, the distinct buckling phenomena alluded to above are identified by quantifying the buckling times for the step pressure loading. Systematic responses are identified and summarized in a behavior map. The main findings of the paper are summarized in Section 5.

2. Formulation of viscoelastic shell theory

2.1. Small-strain, moderate-rotation shell theory with a geometric imperfection

Fig. 1 Schematic of a viscoelastic spherical shell with a Gaussian-shaped imperfection centered at the pole. (a) Coordinates definition $(\theta,\ \omega,\ r)$ and geometry of the shell. (b) A standard linear solid with a free spring of modulus E_∞, and a Maxwell element in parallel with a spring of modulus E_1, and a dashpot of viscosity η.

The small-strain, moderate-rotation theory (Koiter, 1966; Sanders, 1963) is employed for the shell buckling equations. The schematic and coordinates definition $(\theta,\ \omega,\ r)$ are shown in Fig. 1, where θ is the meridional angle, which equals 0 at the equator and $\pi/2$ at the pole, ω is the circumferential angle, and r is the distance from the origin. The middle surface radius, base angle and thickness of the perfect undeformed shell are denoted by R, α_0 and h, respectively. A material point on the middle surface of the undeformed shell with a coordinate $(\theta,\ \omega,\ R)$ will be located on the deformed shell at

$$\bar{\mathbf{r}} = u_\theta \mathbf{i}_\theta + u_\omega \mathbf{i}_\omega + (R+w)\mathbf{i}_r, \tag{1}$$

where $(\mathbf{i}_\theta, \mathbf{i}_\omega,\ \mathbf{i}_r)$ are the unit vectors normal and tangent to the undeformed middle surface, and $(u_\theta, u_\omega,\ w)$ are the corresponding displacements. In this paper, only axisymmetric deflections and imperfections are considered since the essence of spherical shell buckling is captured within this limited class of deformations (Hutchinson, 2016); thus, u_θ and w are only functions of θ, and $u_\omega = 0$.

An axisymmetric dimple-like geometric imperfection $w_I(\theta)$ is introduced at the apex of the perfect shell shown in Fig. 1a. The profile of the imperfection is specified by a Gaussian dimple,

$$w_I = -\delta e^{-(\beta/\beta_I)^2}, \tag{2}$$

where δ is the amplitude of the inward deflection at the apex, $\beta = \pi/2 - \theta$ is the polar angle, and β_I sets the exponential decay width. The tensor equations of Sanders (1963) and Koiter (1966) have been reduced to the classical form for spherical shells, and the derivation of the middle surface strains and bending strains for spherical shells with an imperfection undergoing non-axisymmetric deformation based on the small-strain, moderate-rotation theory is listed in the papers of Hutchinson (2016) and Lee et al. (2016). The corresponding non-zero middle surface strains and bending strains under axisymmetric deformation are

$$\begin{aligned} E_{\omega\omega} &= W - (\varphi + W_{,\theta})\tan\theta, \\ E_{\theta\theta} &= W + \varphi_{,\theta} + W_{,\theta\theta} + \frac{1}{2}\varphi^2 - W_{I,\theta}\varphi, \\ K_{\omega\omega} &= -\frac{1}{R}\varphi\tan\theta, \\ K_{\theta\theta} &= \frac{1}{R}\varphi_{,\theta}, \end{aligned} \tag{3}$$

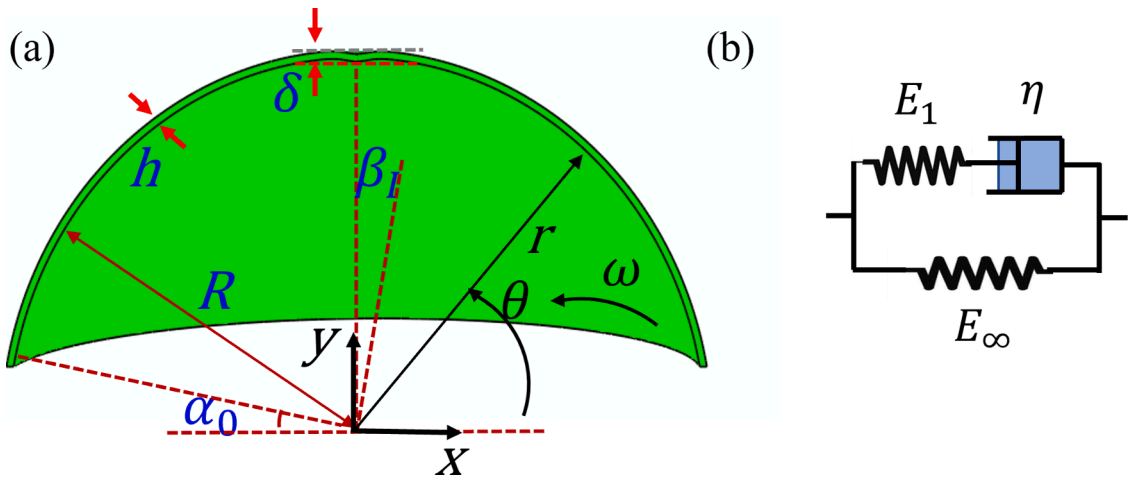

Fig. 1. Schematic of a viscoelastic spherical shell with a Gaussian-shaped imperfection centered at the pole. (a) Coordinates definition $(\theta,\ \omega,\ r)$ and geometry of the shell. (b) A standard linear solid with a free spring of modulus E_∞, and a Maxwell element in parallel with a spring of modulus E_1, and a dashpot of viscosity η.

where the dimensionless displacements and rotation are defined as

$$W = \frac{w}{R}, \varphi = -\frac{w_{,\theta}}{R} + \frac{u_\theta}{R}, U_\theta = \frac{u_\theta}{R}, W_I = \frac{w_I}{R}, \tag{4}$$

with the subscripts '$_{,\theta}$' and '$_{,\theta\theta}$' as the first and second derivatives with respect to θ, respectively, and φ is the rotation. In deriving Eq. (3), the second equation in Eq. (4) has been used to express u_θ in terms of W and φ, which are regarded as the independent variables. Consequently, the strain at an arbitrary position of the shell can be expressed as $\varepsilon_{\alpha\beta} = E_{\alpha\beta} + zK_{\alpha\beta}$, where z is the coordinate in the thickness direction of the shell and measured from the middle surface.

2.2. Viscoelastic constitutive relations

To formulate the viscoelastic shell theory, the time/rate-dependent constitutive equations of viscoelasticity are developed in this section. The Boltzmann superposition principle, stating that the compound response of a material is the sum of the responses to individual loads, is adopted. The stress at time t is the summation of the stress increments at earlier time intervals $d\tau$. The two-dimensional stress-strain relations of viscoelasticity under plane stress can be written as:

$$\sigma_{\alpha\beta} = \frac{1}{1+\nu}\int_0^t E(t-\tau)\dot{\varepsilon}_{\alpha\beta}d\tau + \frac{\nu}{1-\nu^2}\int_0^t E(t-\tau)\dot{\varepsilon}_{\gamma\gamma}\delta_{\alpha\beta}d\tau \tag{5}$$

where E is the modulus, which evolves with time, ν is the Poisson's ratio, which is assumed to be constant, and $\dot{\varepsilon}_{\alpha\beta} = d\varepsilon_{\alpha\beta}/d\tau$. The Greek indices α & β take on values 1 & 2 corresponding to θ & ω, and a repeated Greek index is summed over 1 and 2.

Specifically, the standard linear solid model (Fig. 1b), which is a special case of the generalized Maxwell-Wiechert model (Lakes, 1998), is used to describe the material viscoelasticity. It can capture both relaxation and creep with the minimum number of Maxwell elements. It consists of a free spring with a modulus E_∞, a Maxwell element in parallel with a spring of modulus E_1, and a dashpot of viscosity η. As a result, the modulus of a standard linear solid shows exponential decay with time during relaxation, $E(t) = E_\infty + E_1 e^{-\frac{E_1}{\eta}t}$. Substituting the time-dependent modulus $E(t)$ into Eq. (5) gives

$$\begin{aligned}\sigma_{\alpha\beta} &= \frac{1}{1+\nu}\int_0^t \left(E_\infty + E_1 e^{-\frac{E_1}{\eta}(t-\tau)}\right)\dot{\varepsilon}_{\alpha\beta}d\tau + \frac{\nu}{1-\nu^2}\int_0^t \left(E_\infty + E_1 e^{-\frac{E_1}{\eta}(t-\tau)}\right)\dot{\varepsilon}_{\gamma\gamma}\delta_{\alpha\beta}d\tau \\ &= \frac{1}{1+\nu}\left[(E_\infty + E_1)\varepsilon_{\alpha\beta} - \int_0^t \frac{E_1^2}{\eta}e^{-\frac{E_1}{\eta}(t-\tau)}\varepsilon_{\alpha\beta}d\tau\right] + \frac{\nu}{1-\nu^2}\left[(E_\infty + E_1)\varepsilon_{\gamma\gamma}\delta_{\alpha\beta} - \int_0^t \frac{E_1^2}{\eta}e^{-\frac{E_1}{\eta}(t-\tau)}\varepsilon_{\gamma\gamma}\delta_{\alpha\beta}d\tau\right].\end{aligned} \tag{6}$$

The resultant membrane stresses and the bending moments can be derived by integrating the stresses through the thickness,

$$\begin{aligned}N_{\alpha\beta} &= \int_{-\frac{h}{2}}^{\frac{h}{2}} \sigma_{\alpha\beta}dz, \\ M_{\alpha\beta} &= \int_{-\frac{h}{2}}^{\frac{h}{2}} \sigma_{\alpha\beta}z dz.\end{aligned} \tag{7}$$

For a shell specialized to axisymmetric deformations, the non-zero resultant membrane stresses are $N_{\omega\omega}$, and $N_{\theta\theta}$, while the non-zero bending moments are $M_{\omega\omega}$, and $M_{\theta\theta}$:

$$\begin{aligned}N_{\omega\omega} &= \frac{h}{1-\nu^2}(E_\infty + E_1)(E_{\omega\omega} + \nu E_{\theta\theta}) - \frac{h}{1-\nu^2}\int_0^t \frac{E_1^2}{\eta}e^{-\frac{E_1}{\eta}(t-\tau)}(E_{\omega\omega} + \nu E_{\theta\theta})d\tau, \\ N_{\theta\theta} &= \frac{h}{1-\nu^2}(E_\infty + E_1)(E_{\theta\theta} + \nu E_{\omega\omega}) - \frac{h}{1-\nu^2}\int_0^t \frac{E_1^2}{\eta}e^{-\frac{E_1}{\eta}(t-\tau)}(E_{\theta\theta} + \nu E_{\omega\omega})d\tau, \\ M_{\omega\omega} &= \frac{h^3}{12(1-\nu^2)}(E_1 + E_\infty)(K_{\omega\omega} + \nu K_{\theta\theta}) - \frac{h^3}{12(1-\nu^2)}\int_0^t \frac{E_1^2}{\eta}e^{-\frac{E_1}{\eta}(t-\tau)}(K_{\omega\omega} + \nu K_{\theta\theta})d\tau, \\ M_{\theta\theta} &= \frac{h^3}{12(1-\nu^2)}(E_1 + E_\infty)(K_{\theta\theta} + \nu K_{\omega\omega}) - \frac{h^3}{12(1-\nu^2)}\int_0^t \frac{E_1^2}{\eta}e^{-\frac{E_1}{\eta}(t-\tau)}(K_{\theta\theta} + \nu K_{\omega\omega})d\tau.\end{aligned} \tag{8}$$

It is convenient to normalize these equations as

$$
\begin{aligned}
n_{\omega\omega} &= \frac{12R^2 cos\theta}{h^2\left(1-\nu^2\right)}\left(E_{\omega\omega}+\nu E_{\theta\theta}-E_{rel}\int_0^T e^{-\left(T-\tau^{prime}\right)}\left(E_{\omega\omega}+\nu E_{\theta\theta}\right)d\tau^{prime}\right),\\
n_{\theta\theta} &= \frac{12R^2 cos\theta}{h^2\left(1-\nu^2\right)}\left(E_{\theta\theta}+\nu E_{\omega\omega}-E_{rel}\int_0^T e^{-\left(T-\tau^{prime}\right)}\left(E_{\theta\theta}+\nu E_{\omega\omega}\right)d\tau^{prime}\right),\\
m_{\omega\omega} &= R\cos\theta\left(K_{\omega\omega}+\nu K_{\theta\theta}-E_{rel}\int_0^T e^{-\left(T-\tau^{prime}\right)}\left(K_{\omega\omega}+\nu K_{\theta\theta}\right)d\tau^{prime}\right),\\
m_{\theta\theta} &= R\cos\theta\left(K_{\theta\theta}+\nu K_{\omega\omega}-E_{rel}\int_0^T e^{-\left(T-\tau^{prime}\right)}\left(K_{\theta\theta}+\nu K_{\omega\omega}\right)d\tau^{prime}\right),
\end{aligned}
\tag{9}
$$

with

$$
\begin{aligned}
&t_v=\frac{\eta}{E_1}, E_{rel}=\frac{E_1}{E_1+E_\infty}, T=\frac{t}{t_v}, \tau^{prime}=\frac{\tau}{t_v}, D=\frac{(E_1+E_\infty)h^3}{12(1-\nu^2)},\\
&(m_{\omega\omega},m_{\theta\theta})=\frac{R\cos\theta}{D}(M_{\omega\omega},M_{\theta\theta}),(n_{\omega\omega},n_{\theta\theta})=\frac{R^2\cos\theta}{D(1-\nu^2)}(N_{\omega\omega},N_{\theta\theta}),
\end{aligned}
\tag{10}
$$

where E_{rel} measures the modulus in the Maxwell element relative to the modulus governing rapid straining. The viscoelastic timescale t_v is defined as the ratio of the material viscosity η to modulus E_1 in the Maxwell element, which is used to scale the time.

2.3. Principle of virtual work and equilibrium equations

To enforce the principle of virtual work, the virtual normal displacement and rotation of the middle surface are indicated as δW and $\delta\varphi$, and the associated virtual strains are $\delta\varepsilon_{\alpha\beta}=\delta E_{\alpha\beta}+z\delta K_{\alpha\beta}$. The internal virtual work of the shell can be expressed as

$$
IVW=\int_S dS\int_{-\frac{h}{2}}^{\frac{h}{2}} dz\sigma_{\alpha\beta}\delta\varepsilon_{\alpha\beta}=\int_S\left(N_{\alpha\beta}\delta E_{\alpha\beta}+M_{\alpha\beta}\delta K_{\alpha\beta}\right)dS,
\tag{11}
$$

where S denotes the area of the middle surface with $dS=2\pi R^2 cos\theta d\theta$ for a spherical shell.

When the shell is subjected to a uniform inward pressure p in the radius direction, the external virtual work is

$$
EVW=\int_s pR\delta W dS+\oint_C\left[Q\delta W+T_\theta\delta U_\theta-M_n\delta W_{,n}\right]Rds.
\tag{12}
$$

where Q is the normal edge force, T_θ is the in-plane edge resultant traction, C is the boundary, and s denotes the length of the edge of the shell. M_n is the component of the edge moment, $M_n=M_{\alpha\beta}n_\alpha n_\beta$, where the vector $\boldsymbol{n}$ is the normal to the edge tangent to the shell.

Next, the equilibrium equations are derived from the principle of virtual work, which states that IVW=EVW for all admissible δW and $\delta\varphi$. The divergence theorem is applied to convert the equations to the form that permits identification of independent variations. Besides the dimensionless variables and parameters defined in Eq. (10), a normalized pressure is introduced as

$$
\widetilde{p}=\frac{R^3\cos\theta}{D}p.
\tag{13}
$$

The equilibrium equations are obtained as (see Appendix A for details)

$$
\begin{aligned}
&m_{\theta\theta,\theta\theta}+\left(\tan\theta m_{\omega\omega}\right)_{,\theta}-\left(1-\nu^2\right)\left[n_{\omega\omega}+n_{\theta\theta}+\left(n_{\theta\theta}\left(\varphi-W_{I,\theta}\right)\right)_{,\theta}\right]+\widetilde{p}=0,\\
&m_{\theta\theta,\theta}+\tan\theta m_{\omega\omega}+\left(1-\nu^2\right)\left(n_{\omega\omega}\tan\theta+n_{\theta\theta,\theta}-n_{\theta\theta}\left(\varphi-W_{I,\theta}\right)\right)=0.
\end{aligned}
\tag{14}
$$

Finally, we take the time derivative of the above equilibrium equations, which can be expressed in terms of φ and W through the constitutive equations Eq. (9) and the strain–displacement relations Eq. (3). Only the terms related to the highest order of the unknowns are expanded explicitly; the other terms are readily computed in the numerical code. The equilibrium equations for the time rates of change become

$$
\begin{aligned}
\dot{\varphi}_{,\theta\theta\theta} \;=\; & -\frac{1}{A}\Big[\dot{C}-2\tan\theta\left(\dot{m}_{\theta\theta,\theta}+\tan\theta\dot{m}_{\theta\theta}\right)-\dot{m}_{\theta\theta}+\left(\tan\theta\dot{m}_{\omega\omega}\right)_{,\theta} \\
& +\dot{m}_{\theta\theta,\theta}\left(\varphi-W_{I,\theta}\right)+m_{\theta\theta,\theta}\dot{\varphi}+\tan\theta\dot{m}_{\omega\omega}\left(\varphi-W_{I,\theta}\right)+\tan\theta m_{\omega\omega}\dot{\varphi} \\
& -(1-\nu^2)\left[\dot{n}_{\omega\omega}+\dot{n}_{\theta\theta}+\dot{n}_{\theta\theta}\left(\varphi_{,\theta}-W_{I,\theta\theta}\right)+n_{\theta\theta}\dot{\varphi}_{,\theta}-\dot{n}_{\omega\omega}\tan\theta\left(\varphi-W_{I,\theta}\right)\right. \\
& \left.-n_{\omega\omega}\tan\theta\dot{\varphi}+\dot{n}_{\theta\theta}\left(\varphi-W_{I,\theta}\right)^2+2n_{\theta\theta}\left(\varphi-W_{I,\theta}\right)\dot{\varphi}\right]+\ddot{\tilde{p}}\Big] \\
& +\frac{A}{A^2}\Big[C-2\tan\theta\left(m_{\theta\theta,\theta}+\tan\theta m_{\theta\theta}\right)-m_{\theta\theta}+\left(\tan\theta m_{\omega\omega}\right)_{,\theta}+m_{\theta\theta,\theta}\left(\varphi-W_{I,\theta}\right) \\
& +\tan\theta m_{\omega\omega}\left(\varphi-W_{I,\theta}\right)-\left(1-\nu^2\right)\left[n_{\omega\omega}+n_{\theta\theta}+n_{\theta\theta}\left(\varphi-W_{I,\theta}\right)_{,\theta}\right. \\
& \left.-n_{\omega\omega}\tan\theta\left(\varphi-W_{I,\theta}\right)+n_{\theta\theta}\left(\varphi-W_{I,\theta}\right)^2\right]+\tilde{p}\Big] \\
\dot{W}_{,\theta\theta\theta} \;=\; & -\left(W_{,\theta}+\varphi_{,\theta\theta}+\dot{\varphi}\varphi_{,\theta}+\varphi\dot{\varphi}_{,\theta}-W_{I,\theta}\dot{\varphi}_{,\theta}-W_{I,\theta\theta}\dot{\varphi}\right) \\
& +\frac{1}{B}\left[\dot{D}-\tan\theta\left(1-\nu^2\right)\dot{n}_{\theta\theta}+\dot{m}_{\theta\theta,\theta}+\tan\theta\dot{m}_{\omega\omega}\right. \\
& \left.+(1-\nu^2)\left(\dot{n}_{\omega\omega}\tan\theta-\dot{n}_{\theta\theta}\left(\varphi-W_{I,\theta}\right)-n_{\theta\theta}\dot{\varphi}\right)\right] \\
& -\frac{\dot{B}}{B^2}\left[\dot{D}-\tan\theta\left(1-\nu^2\right)n_{\theta\theta}+m_{\theta\theta,\theta}+\tan\theta m_{\omega\omega}\right. \\
& \left.+(1-\nu^2)\left(n_{\omega\omega}\tan\theta-n_{\theta\theta}\left(\varphi-W_{I,\theta}\right)\right)\right],
\end{aligned}
\tag{15}
$$

with the definition of

$$
A=\cos\theta\left(1-E_{rel}\int_0^T e^{-(T-\tau)}d\tau\right),\ B=-\frac{12R^2}{h^2}A,\ C=R\nu K_{\omega\omega,\theta\theta}A,\ D=\frac{12R^2}{h^2}\nu E_{\omega\omega,\theta}A. \tag{16}
$$

The present formulation describing the deformation of viscoelastic spherical shells with geometric imperfections has led to a system of nonlinear ordinary differential equations (ODEs), which will be solved using the finite difference method and the combined bvp4c solver (a finite difference code that implements the three-stage Lobatto IIIa formula to solve boundary value problems for ODEs) in MATLAB (Kierzenka and Shampine, 2001). The clamped boundary condition requires $W=W_{,\theta}=\varphi=0$ at the base while the analytical nature of the functions W and φ under the axisymmetric condition requires $W_{,\theta}=\varphi=\varphi_{,\theta\theta}=0$ at the pole. And note that numerical approximations are adopted, and high-order terms are neglected when solving the ODEs. Buckling problems under two types of loading are examined in this work: i) a prescribed rate of change of the shell volume and ii) prescribed pressure that is held constant once after it is applied. In addition, the case of a prescribed rate of volume change will be compared with a case that is easier to implement numerically but of less physical interest, a prescribed rate of change of the pole displacement. When the pressure serves as the control variable, the equilibrium equations (Eq. (15)) and viscoelastic constitutive relations (Eq. (9)) are solved with prescribed evolution of pressure with time. When the pole deflection is set as the control parameter, the dimensionless pressure $\widehat{p}=pR^3/D$ is regarded as an

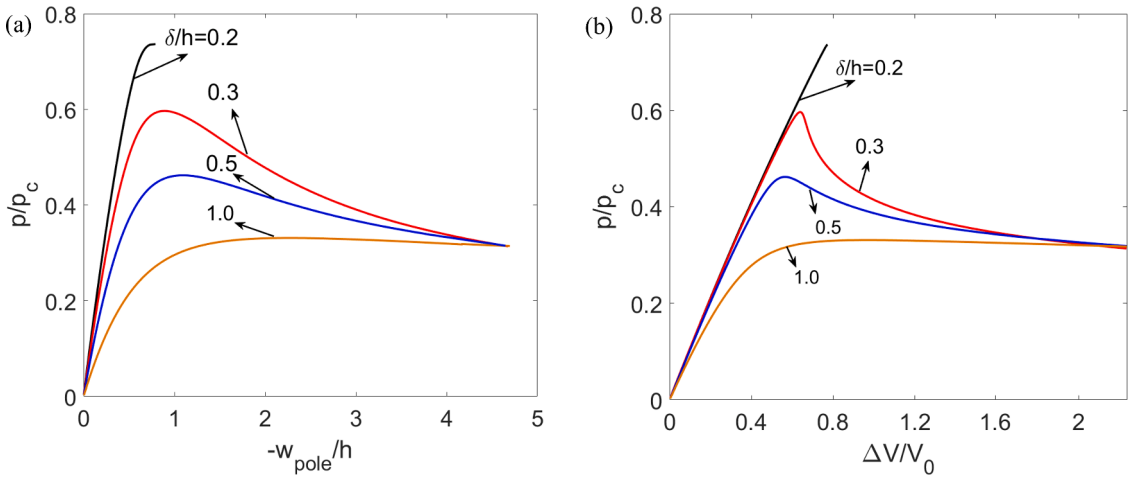

Fig. 2. Effect of the imperfection amplitude δ/h on the load-carrying behavior of viscoelastic shells with E_{rel}=0.4, under a high rate of volume change, $\gamma_v=0.9623$, and with the other parameters fixed at values used throughout the paper: $\alpha_0=\pi/3$, $R/h=50$, $\beta_I=10^\circ$, $\nu=0.5$. (a) Normalized pressure versus normalized displacement at the pole. (b) Normalized pressure as a function of normalized volume change. For the smallest imperfection shown, $\delta/h=0.2$, snap back behavior occurs when $p\cong p_{max}$ and those curves are terminated there.

extra unknown with an additional ODE $d\hat{p}/d\theta = 0$ added to the set of equations, Eqs. (15) and (9). The deformation of the shell can be obtained numerically if dynamic snapping does not occur, which would require consideration of inertia. Volume control is achieved by setting the volume of the shell as an additional variable and adding an extra constraining ODE relating the volume and deflection to the equation set. The pressure is again treated as an extra unknown variable. The procedure under volume control also behaves well until conditions for dynamic snapping are attained.

3. Rate-dependent buckling behaviors

In this section, we begin by investigating the effects of geometric imperfections on buckling pressure of viscoelastic shells. It is known that the classical prediction for the critical buckling pressure of a perfect elastic hemi-spherical shell with $\alpha_0 = \pi/2$ under uniform pressure loading is only slightly different from the result for a full spherical shell (Zoelly, 1915), $p_c = 2E(h/R)^2/\sqrt{3(1-\nu^2)}$, where E is the Young's modulus for the elastic shell. The precise value for the hemispherical shell depends on whether it is clamped or simply supported at the equator. The critical buckling pressure of imperfect shells can be significantly reduced below p_c due to the imperfection sensitivity of shell buckling, which leads to large knockdown factors observed experimentally (Evkin and Lykhachova, 2017; Gerasimidis et al., 2018; Hutchinson and Thompson, 2017, 2018; Karman and Tsien, 1939; Koga and Hoff, 1969; Koiter, 1969; Krenzke and Kiernan, 1963; Lee et al., 2016; Liu et al., 2021; NASA, 1969). For the dimple imperfections of the type considered in this paper, buckling is localized at the pole, and the boundary conditions at the equator, or at other values of α_0, have no influence on the buckling pressure if they are sufficiently strong and if the shell is sufficiently deep, which typically corresponds to the dimensionless parameter $[12(1-\nu^2)]^{1/4}\cos(\alpha_0)\sqrt{R/h} > 3$ (Evkin and Lykhachova, 2019; Huang, 1965; NASA, 1969). In this paper, the ratio of the buckling pressure, the maximum pressure the shell can support p_{max}, to p_c is used to quantify the discrepancy of the actual buckling pressure from the theoretical prediction; in the formula for p_c the initial modulus $(E_1 + E_\infty)$ for the viscoelastic material governing fast straining is used to replace the elastic modulus E of an elastic material to define a reference critical buckling pressure, i.e.,

$$p_c = \frac{2(E_1 + E_\infty)}{\sqrt{3(1-\nu^2)}}\left(\frac{h}{R}\right)^2. \tag{17}$$

3.1. Buckling under a prescribed volume change

We first examine the effect of imperfections on the loading-carrying behavior of viscoelastic shells under fast loading. For these calculations, the viscoelastic shell is loaded at a high rate of volume change with the time-dependence of the pressure solved as described earlier. The volume change rate is chosen sufficiently large such that the shell material responds elastically with modulus $(E_1 + E_\infty)$, i.e., viscoelastic effects are essentially absent. For purposes that will be clear in what follows, we define two dimensionless loading rates, γ_v measuring rate of volume change and γ_d measuring the rate of the pole displacement:

$$\gamma_v = \frac{d}{\Delta V/V_0}dT \text{ and} \gamma_d = -\frac{dW_{pole}}{dT} \tag{18}$$

where the dimensionless quantities, T and W_{pole}, have been defined earlier, ΔV is defined as the volume change from $t = 0$ to time t, and

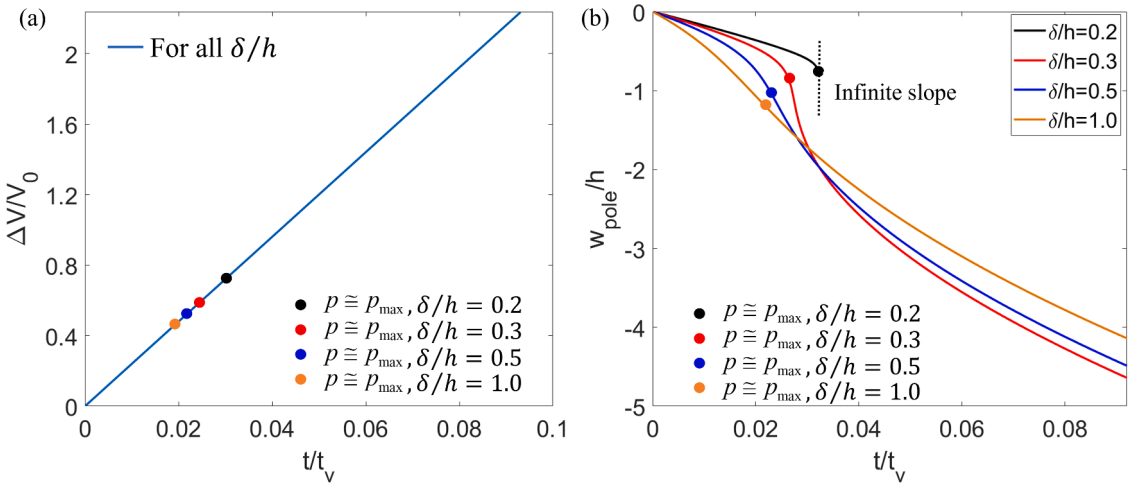

Fig. 3. Volume change and pole displacement with time for the imperfect viscoelastic shells in Fig. 2. (a) Volume change as a function of time for imperfection amplitudes $\delta/h = 0.2,\ 0.3,\ 0.5,\ 1.0$. ΔV is the volume change from $t = 0$ to time t. (b) Normalized displacement at the pole versus normalized time. The computation stops at infinite slope, where $p \cong p_{max}$, for $\delta/h = 0.2$. The additional parameters are those specified earlier and used throughout the paper.

$V_0 = -2\pi R^2 h(1-\sin\alpha_0)/\sqrt{3(1+\nu)/(1-\nu)}$ is an estimate of the volume change for the deep spherical shell associated with the critical pressure in Eq. (17), which ignores the constraint of the clamped boundary in the small boundary layer at the base of the shell.

The plots in Figs. 2 and 3 are computed with a prescribed, rapid rate of volume change, $\gamma_v = 0.9623$, with $E_{rel} = 0.4$. Throughout the paper, the geometric parameters are fixed at $\alpha_0 = \pi/3,\ R/h = 50$ *and* $\beta_I = 10^\circ$, with Poisson's ratio set at $\nu = 0.5$. Note that in this paper, we will not provide the results for perfect and near-perfect shells to avoid numerical singularity and other complex behavior near the buckling, such as localization (Audoly and Hutchinson, 2019). Instead, we will focus on small, but realistic, imperfections with $\delta/h \geq 0.2$. For each choice of imperfection amplitude, $\delta/h = 0.2,\ 0.3,\ 0.5,\ 1$, the normalized pressure, p/p_c, as a function of the displacement at the pole, here normalized by the shell thickness, w_{pole}/h, always first increases, reaches a maximum value, and then decreases monotonically (Fig. 2a). It is well known that the elastic buckling of shells is highly sensitive to imperfections (Koiter, 1969), with an exceptionally dramatic reduction of buckling loads in the range of small imperfections, and this is reflected in Fig. 2. As the imperfection amplitude increases, the buckling pressure further decreases but tends to a plateau. The corresponding pole displacement at the critical pressure increases monotonically but is never much larger than one, or at most two, shell thicknesses at the maximum load point. The fact that shell buckling occurs at such small deflections helps explain why the small-strain, moderate-rotation shell theory is accurate in these applications. Fig. 2b presents results for the same shells but as normalized pressure as a function of normalized volume change, $\Delta V/V_0$. For shells with the smallest imperfection in Fig. 2b ($\delta/h = 0.2$), both p/p_c and $\Delta V/V_0$ decrease along the equilibrium path after attaining the maximum pressure, which is a salient feature of a snapping-back buckling (Budiansky, 1974; Chen and Jin, 2020), indicating that the shell will buckle unstably under either pressure or volume control. For the larger imperfection amplitudes, the critical volume at the onset of buckling becomes smaller, and the post-buckling slope changes from positive to negative, eventually reaching nearly zero. The buckling capacity of the shell is reached in the range of relatively small pole deflections, with the attainment of the maximum pressure occurring when $w_{pole} \cong -h$. In all cases in Figs. 2 and 3, the loading rate, $\gamma_v = 0.9623$, is very high and there is virtually no viscoelastic relaxion. The buckling behavior of these viscoelastic shells is essentially the same as an elastic shell with the short-time modulus $E = E_1 + E_\infty$. Consequently, the results in these figures are essentially identical to those of the elastic shells reported in the literature (Lee et al., 2016). This agreement provides one check on our viscoelastic shell model.

Fig. 3 displays the data in Fig. 2 plotted against dimensionless time, as volume change versus time in Fig. 3a and as pole displacement versus time in Fig. 3b. Because the rate of volume change is prescribed to be constant with $\gamma_v = 0.9623$, the plot in Fig. 3a is simply a straight line, but the points at which the buckling pressure p_{max} is attained for the four imperfection levels is indicated. In Fig. 3b, one can see that for the smallest imperfection, $\delta/h = 0.2$, the curve terminates at the point where snap back would occur under this prescribed rate of volume change. Note in Fig. 2 that the point of maximum pressure is nearly coincident with snap back (the

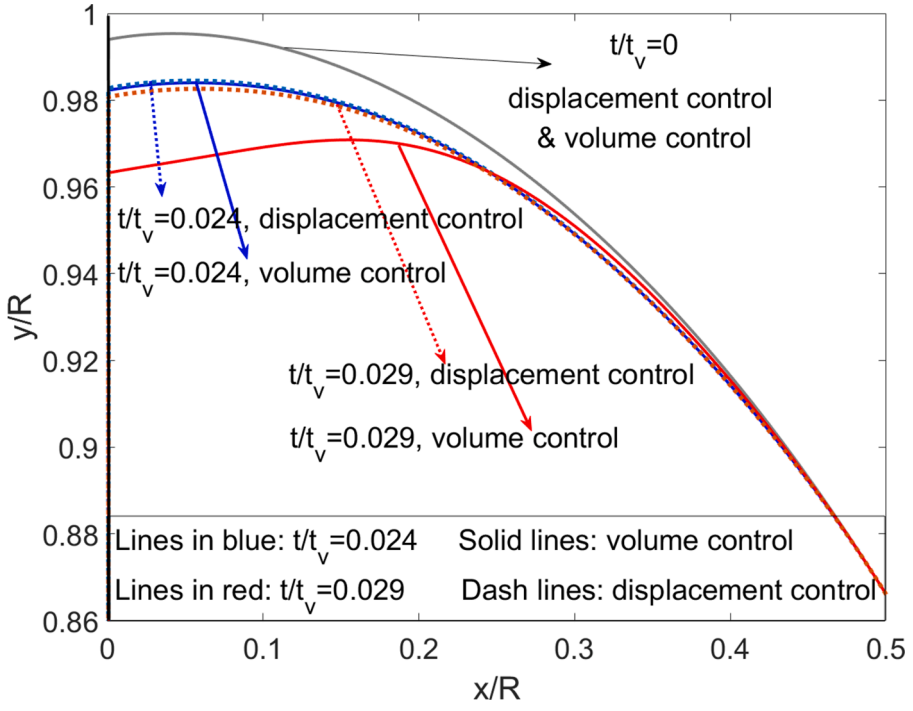

Fig. 4. Middle surface profiles of the initial and deformed states for the imperfect viscoelastic shell with $\delta/h = 0.3$ in Fig. 2 under volume control with $\gamma_v = 0.9623$ compared with those computed using pole displacement control with $\gamma_d = 0.458$. The latter rate is chosen such that the two loading conditions give nearly coincident predictions in the early stages of loading. At $t/t_v = 0.024$, the shells under volume control and displacement control are deformed to almost the same position. At $t/t_v = 0.029$, a sharp increase of the buckling deflection has occurred under volume control, which would be even more dramatic for smaller δ/h, and less so for larger δ/h. No drop exists for displacement control.

maximum pressure is attained just before snap back occurs, which is usually the case for thin shells). The shells with the three larger imperfections have monotonically increasing pole displacements over the time plotted (Fig. 3b), and it can be seen in Fig. 2b that these shells having a prescribed constant rate of volume change do not undergo snap buckling at the maximum pressure. Instead, these shells will undergo stable buckling after the maximum pressure is attained with the buckle amplitude increasing monotonically with the increasing volume change.

Fig. 4 displays the initial and deformed shapes of the middle surface of the imperfect viscoelastic shell with $\delta/h = 0.2$ at three dimensionless times, $t/t_v = 0,\ 0.024,\ 0.029$, for both a fixed rate of volume change ($\gamma_v = 0.9623$) and a fixed rate of pole displacement ($\gamma_d = 0.458$), where x/R and y/R are the normalized coordinates in the cross-section of the shell as defined in Fig. 1. The two rate measures were chosen such that both loadings produced essentially the same rate of volume change in the early stages of loading. Imposing the pole deflection rate is simpler to implement numerically than the volume change rate, and the former leads to a larger range of stable behavior than the latter, as will be seen. However, prescribing the volume change rate is a much more accurate representation of how experiments are typically performed. The initial shape of the shells deviates slightly, but visibly, from the perfectly spherical shape due to the initial imperfection. In Fig. 4 at $t/t_v = 0.024$ the shapes of the imperfect viscoelastic shells deviate from those of the perfect, consistent with the amplitude of the imperfection, and remain almost identical for the two loading conditions. However, in the time between 0.024 and 0,029, the pole displacement of the shell subjected to a fixed rate of prescribed volume change undergoes a sharp increase in the buckle deflection (c.f., Fig. 3b) while the shell with a prescribed rate of pole displacement undergoes a much smaller change. Although not shown, at even larger deflections when the pole displacement is larger than about $w_{pole}/R = 0.1$, the vicinity of the pole is approximately an inverted cap with radius of curvature $-R$.

The viscoelastic material exhibits time- and rate-dependent behavior, which are expected to result in new features of shell buckling. In this paper, the load-carrying behavior of viscoelastic shells is examined over a wide range of loading rates, from extremely slow loading ($\gamma_v = 0.0067$) to extremely fast loading ($\gamma_v = 0.9608$). As a comparison, buckling results for shells having strictly elastic material are also generated. The isotropic linearly elastic material law is employed for the elastic shell, i.e.,

$$N_{\alpha\beta} = \frac{Eh}{(1-\nu^2)}\left[(1-\nu)E_{\alpha\beta} + \nu E_{\gamma\gamma}\delta_{\alpha\beta}\right],$$
$$M_{\alpha\beta} = \frac{Eh^3}{12(1-\nu^2)}\left[(1-\nu)K_{\alpha\beta} + \nu K_{\gamma\gamma}\delta_{\alpha\beta}\right], \tag{19}$$

and solved together with the equilibrium equations (Eq. (14)) and strain-displacement relations (Eq. (3)).

For viscoelastic spherical shells undergoing a wide range of fixed rates of volume change, strong strain-rate-dependency of the buckling pressure is observed in the plots of $p/p_c vs.\ -w_{pole}/h$ in Fig. 5a and in the companion plots of $p/p_c vs.\ \Delta V/V_0$ in Fig. 5b. The maximum normalized pressure, p/p_c, increases with the increase of the loading rate due to the reduction of relaxation, clearly indicating that higher pressures are required to buckle a viscoelastic shell under a higher strain rate. Stated otherwise, the buckling pressure can be substantially reduced when the shell is loaded slowly and as much time is allowed under load as needed. Two asymptotic limits of buckling pressure are relevant. For this example, at the slower loading rates ($\gamma_v = 0.0067$ & 0.0097), the time to attain the maximum pressure is 3 to 4 times the viscoelastic timescale, i.e., $T \cong 3$ or 4, as seen in the companion plot in Fig. 6, where the time-dependence of the pole displacement of these shells is presented. The time to deform the shell to displacements much larger than those at the maximum pressure, such as $-w_{pole}/R = 0.1$ for example, is approximately 10 to 15 times the viscoelastic timescale as seen in Fig. 6. In these two cases, almost full relaxation occurs, and the response is governed by the long-term modulus, E_∞. As a result, the plots $p/p_c vs.\ -w_{pole}/h$ (Fig. 5a) and $p/p_c vs.\ \Delta V/V_0$ (Fig. 5b) approach those of the elastic shell computed with modulus $E = E_\infty$. On the

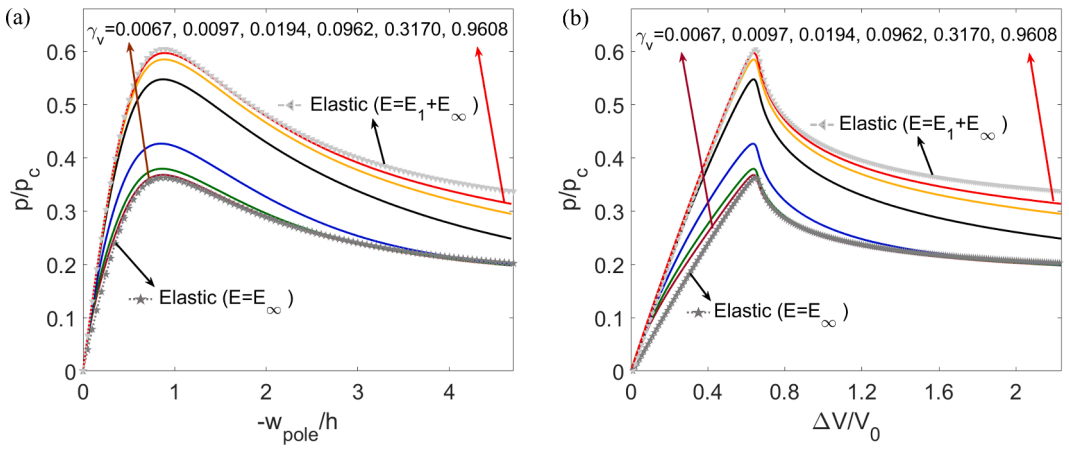

Fig. 5. Rate-dependent buckling behaviors of elastic and viscoelastic shells (E_{rel}=0.4, $\delta/h = 0.3$) under different volume control loading rates ($\gamma_v = 0.0067 \sim 0.9608$). (a) Normalized pressure versus the normalized displacement at the pole. (b) Normalized pressure as a function of the normalized volume change. The additional parameters are those specified earlier and used throughout the paper.

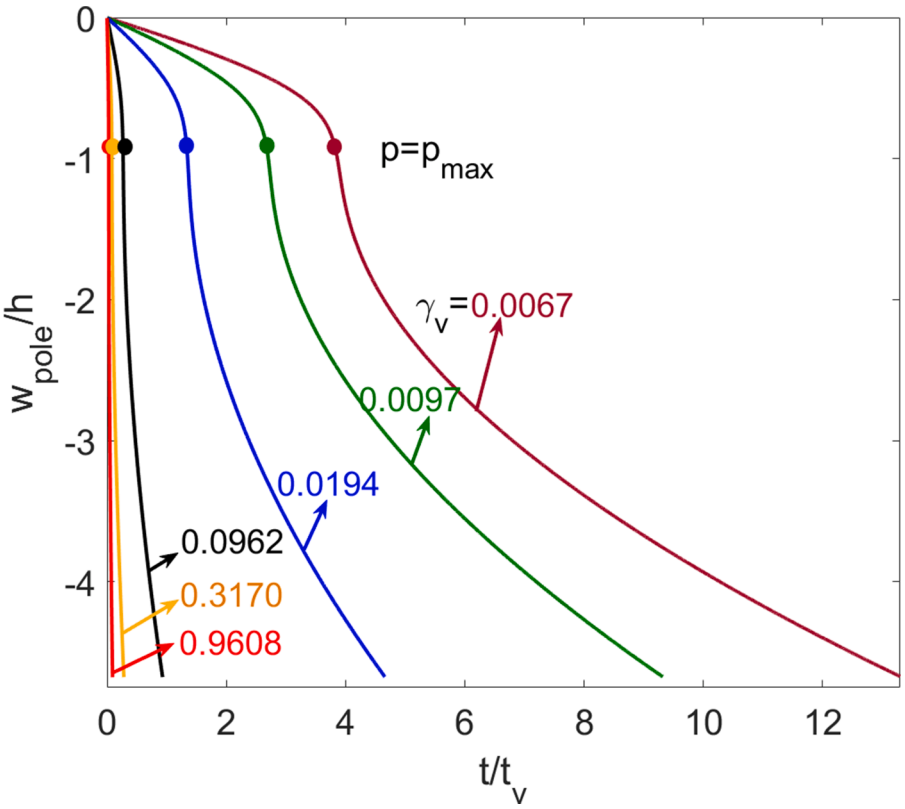

Fig. 6. Normalized displacement at the pole versus normalized time for the viscoelastic shells in Fig. 5 under different loading rates (γ_v = 0.0067 ~ 0.9608).

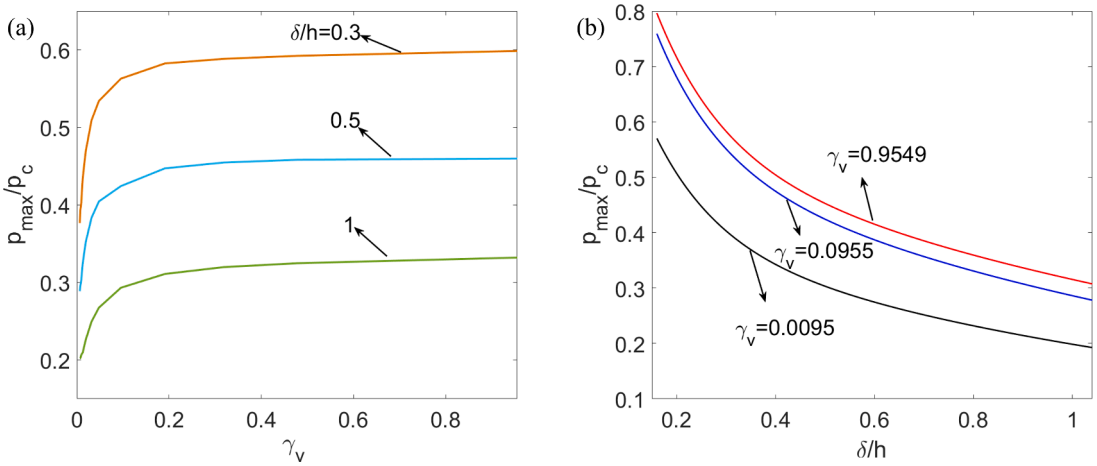

Fig. 7. The influence of imperfection and loading rate on the normalized buckling pressure p_{max}/p_c of viscoelastic shells (E_{rel}=0.4). (a) Normalized buckling pressure as a function of loading rate for different imperfection amplitudes (δ/h = 0.3, 0.5, 1). (b) Normalized buckling pressure as a function of the imperfection amplitude under different loading rates (γ_v = 0.0095, 0.0955, 0.9549). The additional parameters are those specified earlier and used throughout the paper.

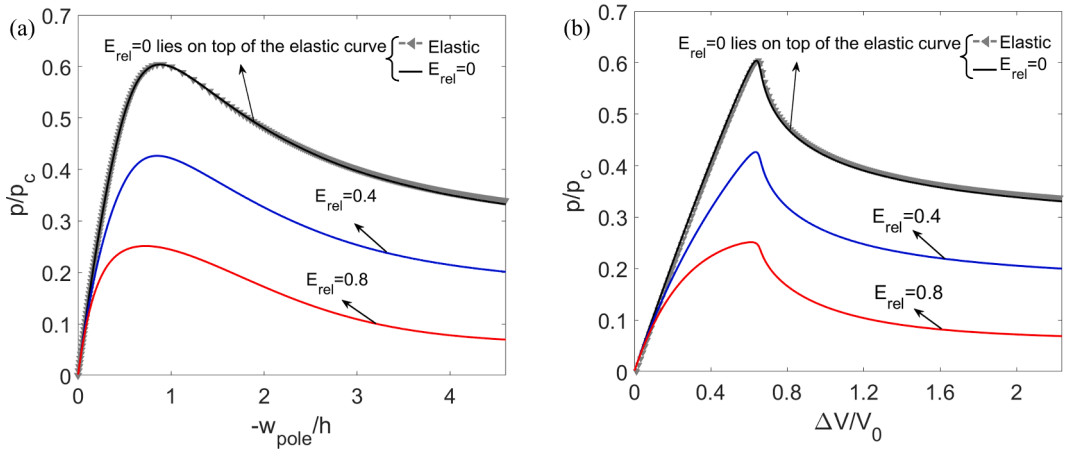

Fig. 8. Effects of material viscoelasticity (E_{rel}=0, 0.4, 0.8) on the loading-carrying behavior of spherical shells subjected to a moderate loading rate $\gamma_v = 0.0194$. (a) Normalized pressure versus normalized displacement at the pole. (b) Normalized pressure as a function of the normalized volume change. The additional parameters are those specified earlier and used throughout the paper.

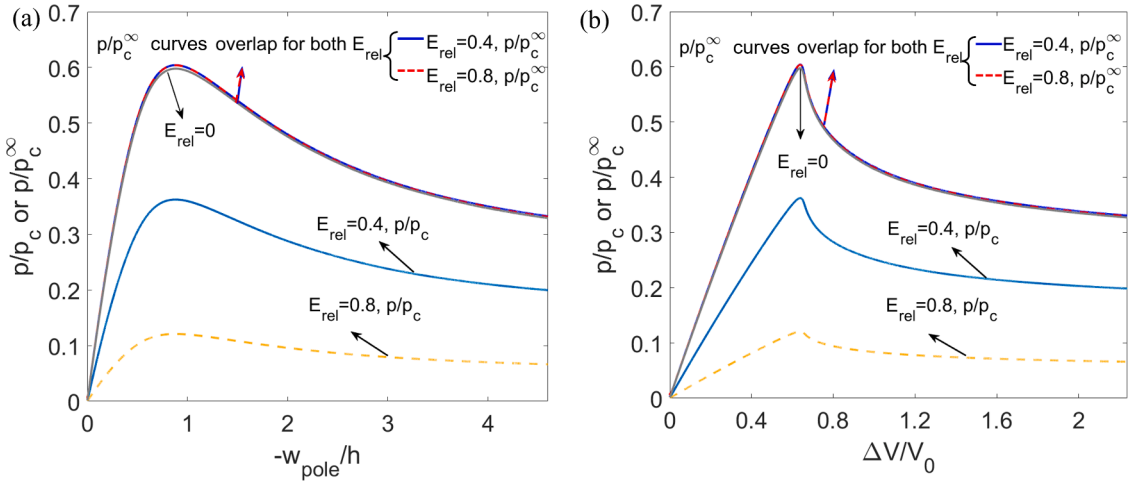

Fig. 9. Effects of material viscoelasticity (E_{rel}=0, 0.4, 0.8) on the load-carrying behavior of shells at an extremely small volume control loading rate ($\gamma_v = 9.62 \times 10^{-5}$), with the pressure normalized by two critical buckling pressures, p_c and p_c^{∞}. The other geometric parameters of the shells are the same as those in Fig. 8. (a) Normalized pressure versus the normalized displacement at the pole. (b) Normalized pressure as a function of the normalized volume change. Blue solid lines and red dash lines are overlapped.

other hand, for the two highest loading rates of $\gamma_v = 0.3170$ & 0.9608, the corresponding dimensionless times are much smaller, and the level of relaxation is smaller. Consequently, the effective modulus of the shell is close to the instantaneous modulus $E_1 + E_\infty$, and the curves for the two high loading rates in Fig. 5 approach those of the elastic shell computed with modulus $E = E_1 + E_\infty$. The maximum pressure occurs at nearly the same value of the pole deflection, i.e., $w_{pole} \cong -h$, for all the loading rates.

The influence of imperfection and loading rate on the normalized buckling pressure $p_{\max}/p_c$ of viscoelastic shells is further revealed in Fig. 7. In Fig. 7a, $p_{\max}/p_c$ increases significantly within the loading rate range $0 < \gamma_v < 0.1$ and then reaches a plateau at larger loading rates. In Fig. 7b, the qualitative dependence of p_{max}/p_c on imperfection amplitude δ/h is similar for all the loading rates. Further insights on this trend will be gained in the investigation of the constant pressure loading. Almost all the increase of magnitude of $p_{\max}/p_c$ occurs when the loading rate increases from 0.0095 to 0.9549. However, as seen in Fig. 7a, the change of $p_{\max}/p_c$ with the loading rate under fixed δ/h is highly nonlinear, because of the exponential decay of the modulus with time.

In Fig. 8 the load-carrying responses of the viscoelastic deep spherical shells are investigated for three relative moduli of relaxation (E_{rel}=0, 0.4, 0.8) under a moderate loading rate $\gamma_v = 0.0194$ to reveal the dependence on E_{rel}. The predictions for an elastic shell computed with $E = E_1 + E_\infty$ are included in this figure. When $E_{rel} = 0$, no relaxation occurs in the material, and the corresponding curves in Fig. 8 almost coincide with those of the elastic shell. Small discrepancies are observed in the vicinity of the peak pressure caused by small numerical errors associated with the difference between the models in the time-dependent and time-independent cases. On the other hand, when E_{rel} increases, notable decreases are observed in p/p_c and there is a small decrease in the pole

displacement and volume at the onset of buckling.

Next, we examine the situation when the shell is deformed under an extremely small loading rate, $\gamma_v = 9.62 \times 10^{-5}$. Under this low loading rate, the effective modulus of the shell is expected to be nearly the long-term nodulus E_∞. Recall that the critical reference buckling pressure, p_c, has been defined using the high strain-rate modulus, $E_1 + E_\infty$, for the viscoelastic shells. To delineate the slow rate limit for the buckling pressure, the 'slow' critical reference bucking pressure is re-defined using E_∞, i.e.,

$$p_c^\infty = \frac{2E_\infty}{\sqrt{3(1-\nu^2)}}\left(\frac{h}{R}\right)^2. \tag{20}$$

We normalize the pressure in two ways, p/p_c and p/p_c^∞, and plot each as a function of $-w_{pole}/h$ and $\Delta V/V_0$ for three values of E_{rel} (Fig. 9). It can be seen that p/p_c for a given $-w_{pole}/h$ or $\Delta V/V_0$ decreases as E_{rel} changes from 0.4 to 0.8, as in the trend in Fig. 8, but it is always lower than the corresponding value in Fig. 8 due to the lower loading rate. However, with the pressure normalized by p_c^∞, curves for different values of E_{rel} (red dashed and dark blue solid lines) overlap, and approach the curves identified by $E_{rel} = 0$ for p/p_c *vs.* $-w_{pole}/h$ (Fig. 9a) and p/p_c *vs.* $\Delta V/V_0$ (Fig. 9b). This indicates that for extremely slow loading, the mechanical behavior of the shell is effectively governed by E_∞, despite different values of E_{rel}.

Before proceeding to discuss spherical shells subjected to step pressure loading, we digress to emphasize that, with the exception of the results for $\Delta V/V_0$, the results for the buckling pressure determined for the specific shell geometry and other parameters plotted in the figures in Section 3.1, as well as those to follow in Sections 3.2 and 4, are approximately independent of both h/R and α_0, assuming the shells are thin, deep and the imperfection width parameter, β_I, scales with $\sqrt{h/R}$. This assertion follows from the extensive study of Hutchinson (2016) using dimensionless parameters. The imperfection scaling is detailed in that earlier reference, and the fact that there is very little dependence on α_0 if the spherical cap is deep follows from the fact that the buckling mode is localized near the pole of the shell, as illustrated in Fig. 4. There is a dependence of $\Delta V/V_0$ on h/R due to the fact that, when the pressure changes, the entire shell undergoes some radial displacement.

3.2. *Buckling under a rapidly applied pressure which is then held constant*

The buckling behavior of viscoelastic spherical shells under prescribed constant rates of volume change has been investigated in the above section. In this section, we will focus on the buckling of viscoelastic shells under a constant prescribed pressure that is lower than

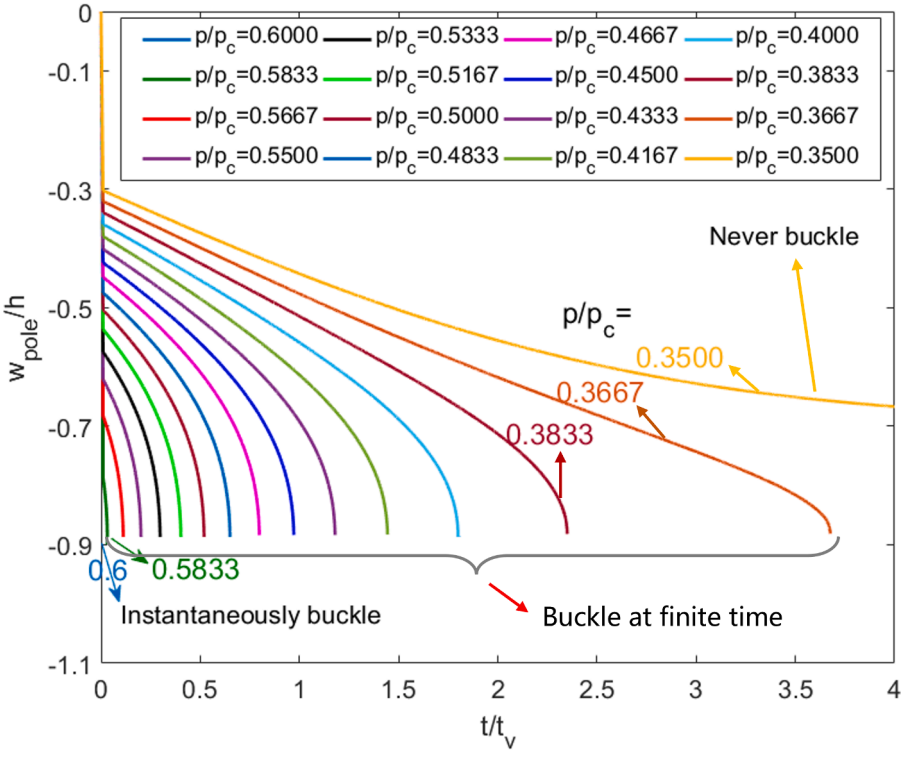

Fig. 10. Pole deflections normalized by the shell thickness, w_{pole}/h, plotted against time for an imperfect viscoelastic shell ($\delta/h = 0.3$, $\beta_I = 10^\circ$) for different external pressures p/p_c from 0.35 to 0.60 that are ramped up rapidly and then held constant. When subjected to different levels of sustained pressures, the shell shows three types of response, including near-instantaneous buckling under sufficiently high pressure, creep buckling under intermediate pressure, and no buckling at sufficiently low pressure.

the maximum pressure p_{max} the shell can support under rapid loading. Stated in another way, we investigate the phenomenon of creep buckling of an imperfect shell of viscoelastic material subjected to steadily applied external pressure. The evolution of the pole deflection and volume change with time for different applied pressures and imperfections is computed, and it will be seen that the buckling behavior of these viscoelastic shells can be classified into three categories.

In the simulations presented in Fig. 10, the external pressure is applied almost instantaneously to a viscoelastic shell ($\alpha_0 = \pi/3$, $R/h = 50$, $\delta/h = 0.3$, $\beta_I = 10^\circ$, $E_{rel} = 0.4$, $\nu = 0.5$) and then held constant. In carrying out the simulations, the pressure is increased from 0 to the final steady value in the short time period $t_{loading}/t_v = 0.01$. Consequently, in the nearly instantaneous ramp-up of the pressure, the shell responds effectively as if it were elastic governed by the fast-loading modulus $E_\infty + E_1$. The constant pressure applied, p/p_c, ranges from 0.35 to 0.6, and it will be seen that a variety of shell buckling phenomena are revealed. The computed pole deflections are plotted as functions of time under different pressures in Fig. 10 for the shell with an imperfection having $\delta/h = 0.3$ that buckles elastically at $p/p_c \cong 0.60$ (with $E = E_1 + E_\infty$). Following the rapid ramp-up, the pole deflection increases over time caused by the creep occurring in the viscoelastic material under constant stress. However, as seen in Fig. 10, the growth rate of the deflection is distinctly different for different pressures. When this shell is subjected to a relatively low pressure ($p/p_c = 0.35$), the growth rate decreases with time, and finally reaches zero, indicating that the shell does not buckle. Non-buckling behavior occurs for pressures below a pressure threshold which depends on the level of imperfection. For pressures somewhat above this threshold, the growth rate of the pole deflection increases with time until it becomes infinite (i.e., a vertical slope in Fig. 10) at a finite time. The shell would undergo snap buckling at this time. This phenomenon is an example of creep buckling as it occurs in imperfection-sensitive shells. The simulations have been terminated at this critical time. The critical time is referred to as the buckling time, $t_{buckling}$. In the range of applied pressures in which creep buckling occurs (approximately $0.36 < p/p_c < 0.58$ for the cases in Fig. 10), the buckling time is a strong function of the applied pressure (see ahead the curve for this imperfection in Fig. 13). The upper end of the pressure range for creep bucking ($p/p_c \cong 0.60$ for the shell in Fig. 10) is the elastic buckling pressure, which in turn is strongly dependent on the level of imperfection, as discussed in more detail later.

Based on the examples discussed above, the time range for the buckling behavior of a shell subjected to a constant applied pressure is divided into three types: essentially instantaneous buckling when the shell buckles elastically at p_{max}, creep buckling when the slope of the w_{pole}/h - t/t_v curve decreases with time and reaches negative infinity at a finite time $t_{buckling}$, and no buckling when the slope of the w_{pole}/h - t/t_v curve increases with time and eventually approaches 0. These results explain the aspects of shell creep buckling observed in experiments (Stein-Montalvo et al., 2021), and they quantify the relationship between the buckling time and pressure. A material point in a viscoelastic shell that is subjected to a constant pressure experiences a reduction in modulus with time, leading to creep of the shell. Even if the instantaneous elastic buckling pressure is higher than the prescribed pressure, the shell may buckle after finite time due to the drift towards the lower effective modulus. If the applied pressure is lower than the buckling pressure for a shell with the long-time modulus E_∞, buckling cannot happen even after long times. By contrast, instantaneous buckling can be expected if the pressure is higher than the buckling pressure for a shell with short time modulus, $E_\infty + E_1$.

The results discussed above have been for a single imperfection ($\delta/h = 0.3$) that causes the shell to buckle instantaneously at $p/p_c \cong 0.60$. The effect of the imperfection amplitude on the buckling process is shown in Fig. 11 with all the other geometric and material parameters unchanged ($\alpha_0 = \pi/3, R/h = 50$, $\beta_I = 10^\circ$, $E_{rel} = 0.4$, $\nu = 0.5$). The relation between the applied steady pressure and the buckling time, $t_{buckling}/t_v$, is shown in Fig. 11a for the imperfection amplitude considered above, $\delta/h = 0.3$, and for a larger imperfection amplitude $\delta/h = 1$. For both imperfection amplitudes in Fig. 11a, the buckling time increases as the applied pressure is lowered below the level causing instantaneous buckling, and the curve reaches a plateau in pressure at buckling times greater than about $t_{buckling}/t_v = 2$ for each of the two imperfection levels shown. For pressures below the plateau, buckling does not occur. Fig. 11b cross-plots the buckling pressure versus the imperfection amplitude for three dimensionless buckling times: short, intermediate and

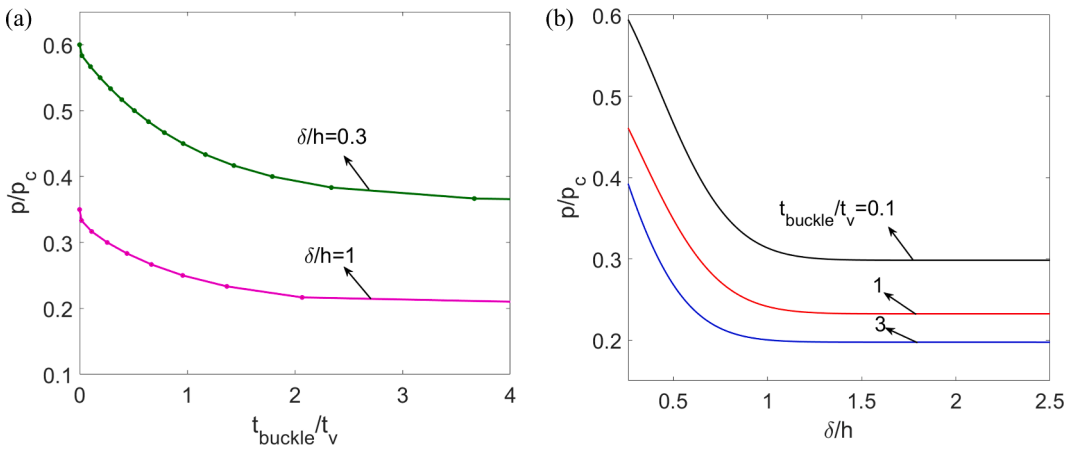

Fig. 11. Relation between prescribed pressure, buckling time and imperfection amplitude for shells subjected to a rapidly applied pressure that is then held constant at p. (a) Pressure versus buckling time for two imperfection amplitudes. (b) Pressure versus imperfection amplitude for three fixed buckling times.

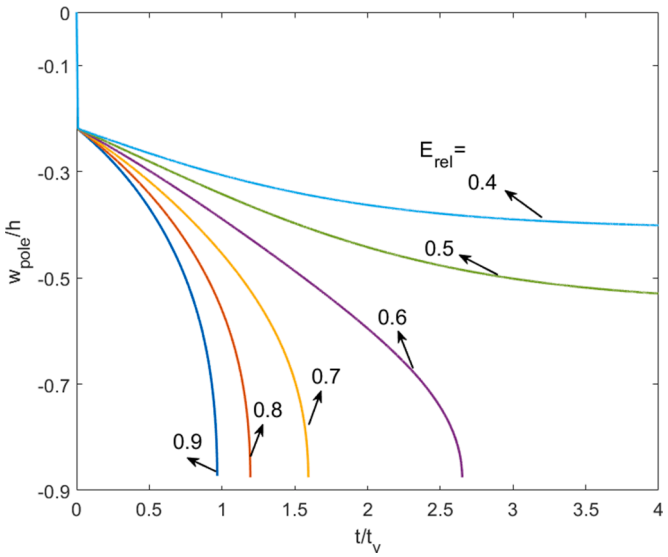

Fig. 12. Pole deflection, w_{pole}/h, as a function of time for different viscoelastic properties (E_{rel}=0.4 to 0.9), when an external pressure $p/p_c = 0.27$ is applied rapidly to the shells and then held constant. The shell has imperfection amplitude, $\delta/h = 0.3$, with other parameters given in the text.

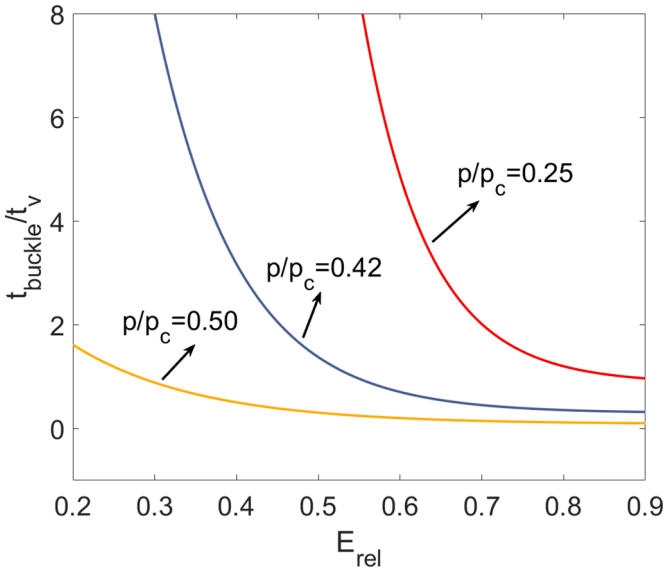

Fig. 13. Normalized buckling time, $t_{buckling}/t_v$, of viscoelastic shells as dependent on E_{rel} and applied pressures. $t_{buckling}/t_v$ versus E_{rel} for three pressure loadings (p/p_c=0.25, 0.42, 0.50) for a shell with imperfection $\delta/h = 0.3$ and other parameters given in the text.

'long'. On each curve, the shell buckles at the time indicated. We have only plotted one curve for 'long' buckling times (the lowest curve in Fig. 11b), but this curve is approximately applicable for pressures applied for all times greater than about $t_{buckling}/t_v = 2$. This is the long-time limit. At a given imperfection amplitude, the shell will never buckle at pressures below the lowest curve. These imperfection-sensitivity curves have features that are qualitatively similar to the corresponding curves for elastic shells. For imperfection amplitudes greater than about $\delta/h = 1$, they level off at a plateau pressure. Of course, the nature of the cross-plot is that the plateau is lower for a longer time allowed for buckling, but the result for $t_{buckling}/t_v = 3$ is essentially the long-time limit.

4. Viscoelastic behavior and a map of buckling behavior for viscoelastic shells subjected to constant pressure

The material viscoelasticity determines the creep buckling behavior of the shells, and this connection is pursued in this section. The viscosity η is embedded in the dimensionless time while the relative modulus, $E_{rel} = E_1/(E_1 + E_\infty)$, is the other dimensionless parameter controlling the time dependence with the limit $E_{rel} = 0$ corresponding to the absence of viscosity and non-zero values of E_{rel}

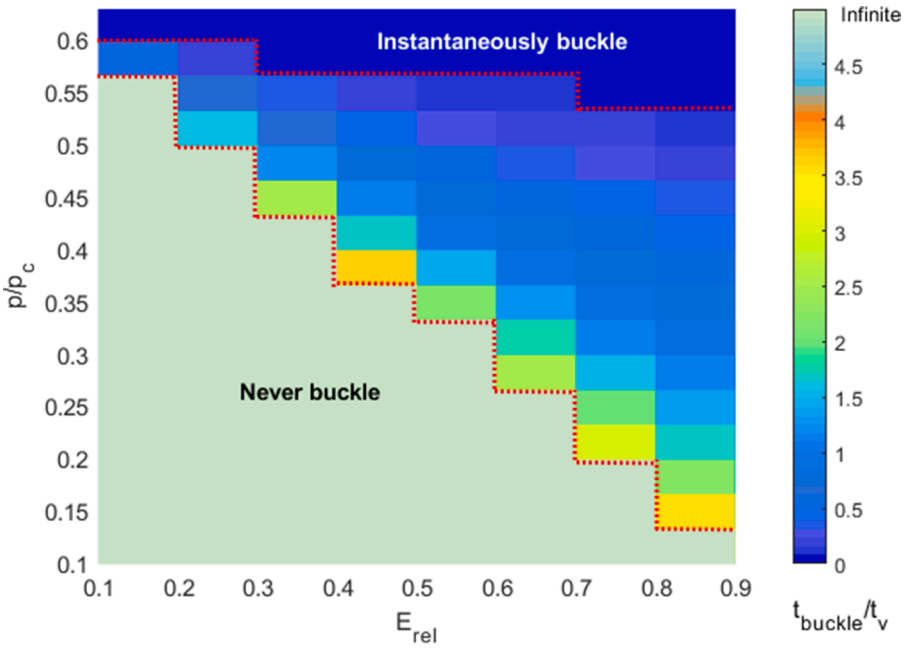

Fig. 14. Buckling modes for viscoelastic shells with imperfection $\delta/h = 0.3$ with respect to the holding pressure p/p_c and material viscoelasticity E_{rel}. The color bar shows $t_{buckling}/t_v$, which changes from 0 to infinity, corresponding to three types of buckling behaviors: near-instantaneous buckling, creep buckling at finite time, and no buckling.

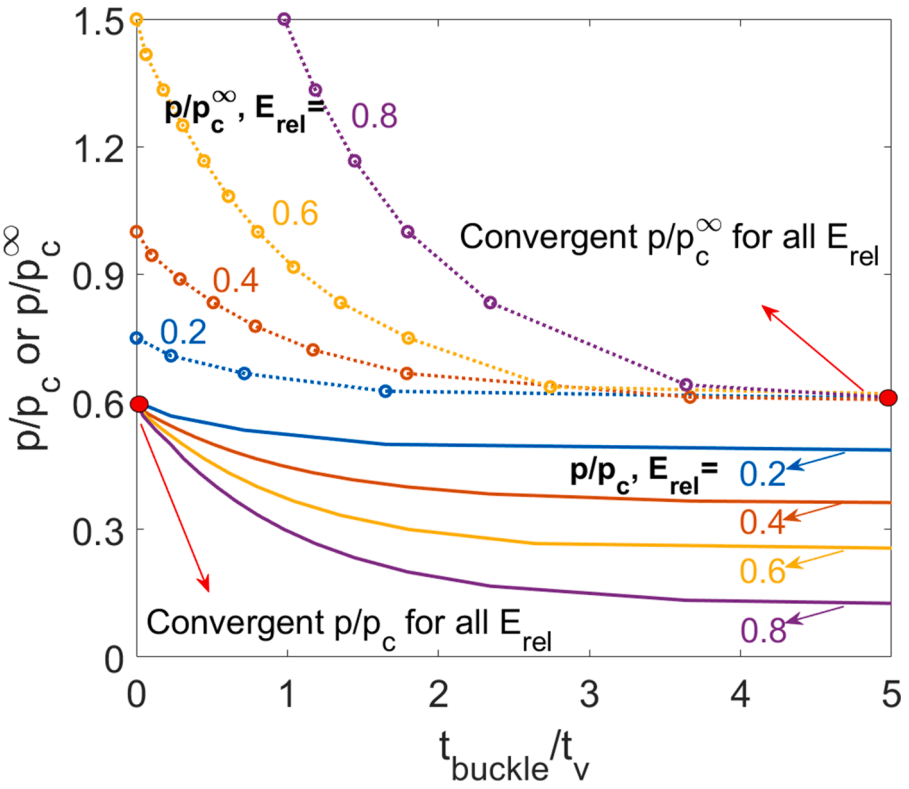

Fig. 15. Two normalizations of the applied pressure (p/p_c and p/p_c^∞) as functions of $t_{buckling}/t_v$ for four values of the relative modulus (E_{rel}=0.2, 0.4, 0.6 and 0.8). The curves of p/p_c *vs.* $t_{buckling}/t_v$ converge for all E_{rel} at $t_{buckling}/t_v = 0$, which is the elastic buckling load for a shell with modulus $E_1 + E_\infty$. The curves of p/p_c^∞ *vs.* $t_{buckling}/t_v$ converge for all E_{rel} at the limit $t_{buckling}/t_v \to \infty$, which is nearly same as the elastic buckling load for a shell with modulus E_∞. The two red dots represent the convergent values for p/p_c and p/p_c^∞.

corresponding to time-dependence. The example presented in Fig. 12 illustrates the influence of E_{rel} on shell responses for pressures that are rapidly applied and then held constant. For all the simulations in Fig. 12, the pressure is p/p_c=0.27 with responses computed for a wide range of the relative modulus, $E_{rel} = 0.4$ to 0.9. The other parameters are those used in the other examples ($\alpha_0 = \pi/3, R/h = 50, \delta/h = 0.3,\ \beta_I = 10^\circ,\ \nu = 0.5$). As in the previous simulations, the initial loading rate is $t_{loading}/t_v$=0.01. The pole deflection as a function of time is plotted for six values of E_{rel}. At the applied pressure and for the imperfection amplitude of the shell in Fig. 12, the shell does not buckle when the relative relaxation is sufficiently low ($E_{rel} \leq$0.5), even after long-term creep, and stabilizes in a deformed configuration that has been influenced by material creep. When E_{rel} is greater than about 0.5 for this example, buckling occurs after a time delay that depends on E_{rel}: the larger E_{rel}, the less time required to buckle. Fig. 12 reveals that even for E_{rel}=0.9 the shell does not buckle until t/t_v approaches approximately 1 under the pressure p/p_c=0.27.

The effect of E_{rel} on $t_{buckling}/t_v$ under three pressures, $p/p_c = 0.25$, 0.42 and 0.50, is further explored (Fig. 13) for the shell with imperfection amplitude $\delta/h = 0.3$. It is seen that, subjected to certain pressures p/p_c, $t_{buckling}/t_v$ can increase without bound as E_{rel} diminishes to a limit depending on the pressure. For values of E_{rel} below this limit, buckling will not occur. Moreover, this limiting value of E_{rel} increases with decreasing p/p_c. For p/p_c=0.25 and 0.42, these limits are roughly $E_{rel} = 0.55$ and $E_{rel} = 0.3$, respectively. The elastic buckling pressure of this shell is about $p/p_c \cong 0.60$ (c.f., Fig. 7a), and thus the limiting value of E_{rel} for the shell subjected to $p/p_c = 0.5$ in Fig. 13 occurs somewhere in the range $E_{rel} = 0$ *to* 0.2, outside the range in which computations were performed.

The effects of the material viscoelasticity (E_{rel}) and holding pressure (p/p_c) on the buckling modes of imperfect viscoelastic shells with $\delta/h = 0.3$ are summarized in Fig. 14. Three types of buckling behavior are explicitly classified by $t_{buckling}/t_v$, including again near-instantaneous buckling, creep bucking at finite time and no buckling. Note that instantaneous buckling here is defined as $t_{buckling}/t_v < 0.05$, which is prone to occur for high values of E_{rel} and p/p_c. On the other hand, shells do not buckle if E_{rel} and p/p_c are relatively small. In the middle region, creep buckling is observed for moderate values of E_{rel} and p/p_c. For a fixed E_{rel}, the buckling mode changes in a sequence from no buckling, creep bucking to instantaneous buckling with the increase of p/p_c. As for a fixed p/p_c in a wide range of $0.1 \leq p/p_c \leq 0.55$, shells only exhibit the mode of no buckling and creep buckling, and near-instantaneous buckling only takes place when $p/p_c \geq 0.55$.

Fig. 15 reveals important insights to time-dependent buckling of viscoelastic shells. As in Fig. 13, the shell has an imperfection amplitude $\delta/h = 0.3$ and it is subjected to a rapidly applied pressure p that is then held constant. In Fig. 15, the applied pressure on the vertical axis is normalized in two ways, p/p_c and p/p_c^∞. The dimensionless time to buckling appears on the horizontal axis. Curves for each of the two pressure normalizations are shown for four values of the relative modulus, $E_{rel} = 0.2$, 0.4, 0.6 and 0.8. Recall that the short-time elastic buckling pressure for the shell with this imperfection is $p/p_c \cong 0.60$, and any pressure exceeding this value will 'instantaneously' collapse the shell. The curves of p/p_c vs. $t_{buckling}/t_v$ in Fig. 15 show that at any pressure below $p/p_c \cong 0.60$ either no buckling occurs or the buckling time is finite, depending on E_{rel}. For every value of E_{rel}, the curves for this normalization converge to the 'short-time' buckling pressure, $p/p_c \cong 0.60$, in the limit of very short loading times. The convergence is expected, as discussed

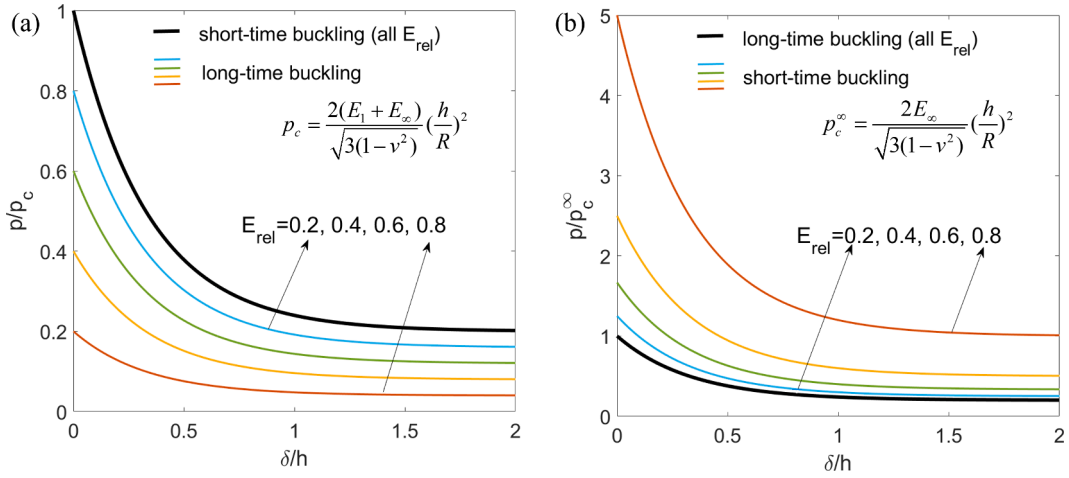

Fig. 16. Two imperfection sensitivity maps presenting the short-time and long-time limits for buckling for pressures that are rapidly applied and then held constant at p. In (a) the normalization p/p_c is used, and in (b) the normalization p/p_c^∞ is used. The construction of the maps is described in the text. In (a), the short-time limit (heavy curve) for instantaneous elastic buckling applies for all E_{rel}, and any pressure on or above this curve produces immediate collapse of the shell. Each of the light curves, corresponding to a specific value of E_{rel}, gives the pressure at which the shell undergoes creep buckling with buckling occurring at the long-time limit. Below this curve (for the given value of E_{rel}), buckling never occurs. For pressures lying between the short-time limit and the long-time limit, creep buckling occurs at some finite time. In (b), the long-time limit (heavy curve) applies for all E_{rel}; for any pressure below this curve buckling never occurs. For pressures lying on or above each of the light curves, for a specific E_{rel}, buckling occurs instantaneously. For pressures lying between the light curve (for the given value of E_{rel}) and the heavy curve, creep buckling occurs at some finite time.

earlier, because for very short buckling times viscous behavior plays essentially no role, and the material responds elastically with modulus $E_1 + E_\infty$, which is the modulus employed in defining p_c in Eq. (17). Now, consider the 'long-time' buckling limit when $t_{buckling}/t_v$ is large and focus on the curves in Fig. 15 that employ the normalization p/p_c^∞. These curves, for each value of E_{rel}, converge for large $t_{buckling}/t_v$ to a common long-time limit, and, moreover, this limit is almost the same numerically as the short-time limit just discussed, but now for the other normalization, i.e., $p/p_c^\infty \cong 0.60$. Recall that p_c^∞, defined in Eq. (20), is the elastic buckling pressure of the perfect shell with the long-time modulus E_∞, and note that

$$p/p_c^\infty = (1 - E_{rel})\, p/p_c. \tag{21}$$

The convergence in the long-time limit of p/p_c^∞ to a buckling pressure that is independent of E_{rel} and equal to the short-time limit expressed as the other normalization can be explained as follows. By Eq. (21), the short-time pressure p/p_c^∞ is always less than p/p_c and thus the shell does not buckle when the pressure is first applied. Correspondingly, because the short-time modulus controls the very early deflections of the shell, those are less than required to buckle the shell. In the ensuing response when the pressure is held constant, the shell creeps and the deflections increase. In the long-time limit, the deflections are determined only by E_∞, with no influence of E_{rel}, and, thus, if p/p_c^∞ equals the short-time limit for buckling, the shell will just reach the buckling condition at large times. The parameters specifying the viscous behavior, E_1 and η have no influence on this limit. While this result can be rationalized by the argument just given, it is a remarkable result. The results in Fig. 15 were computed for a shell with the imperfection amplitude, $\delta/h = 0.3$. We have carried out additional calculations for $\delta/h = 0.5$ and $\delta/h = 1$ to verify that the long-time limit is indeed equal to the short-time limit expressed in the other normalization and independent of E_{rel} for these two other levels of imperfection.

The coincidence of the short-time and long-time limits for the two respective pressure normalizations, independent of E_{rel}, enables a simplified and insightful way of viewing buckling under constant pressure for spherical shells made of viscoelastic materials of the standard linear solid. We construct imperfection-sensitivity maps which divide the pressure range into three regions: instantaneous elastic buckling, time-dependent creep buckling, and no buckling. For plotting the maps, we use the following formulas for the two coincident limits discussed above:

$$\frac{p}{p_c} = 0.2 + 0.8e^{-3\delta/h}\ (\text{short} - \text{time}\ \ \text{limit}) \quad \frac{p}{p_c^\infty} = 0.2 + 0.8e^{-3\delta/h}\ (\text{long} - \text{time}\ \ \text{limit}). \tag{22}$$

The formula, $p/p_c = 0.2 + 0.8e^{-3\delta/h}$, is a realistic representative approximation to the elastic buckling of thin spherical shells with an imperfection at the pole for any h/R, as long as it is sufficiently small so that the shell can be regarded as thin. The buckling pressure plateaus at $p/p_c = 0.2$ for 'large' imperfections. More accurate results depend on full details of the imperfection, as can be found in Hutchinson (2016) and Lee et al. (2016), and the formula used in Eq. (22) can be readily replaced by any other elastic imperfection sensitivity relation.

It is straightforward to generate the imperfection sensitivity plots in Fig. 16 by making use of the relation Eq. (21) between the two pressure normalizations, i.e., $p/p_c^\infty = (1 - E_{rel})p/p_c$. Consider first the plot using the normalization p/p_c in Fig. 16a. In this plot, the short-time limit indicated by the heavy curve is the instantaneous buckling pressure for all E_{rel}. For pressures on or above this curve the shell buckles immediately and catastrophically. The light curves in this plot correspond to the long-time buckling pressure, dependent on E_{rel}. Any pressure below this curve (for a given E_{rel}) does not result in buckling, while any pressure between the heavy curve and the light curve produces creep buckling of the shell at some finite time. The more significant the viscoelasticity, i.e., the larger E_{rel}, the larger the spread between the long-time and short-time limits. The plot in Fig. 16b using the normalization p/p_c^∞ reverses the juxtaposition of the curves. Now, the long-time limit indicated by the heavy curve is independent of E_{rel}, while the light curves representing short-time (instantaneous) elastic buckling depend on E_{rel}. In Fig. 16b, buckling never occurs for pressures below the heavy curve, while buckling is instantaneous for pressures above the light curve (for the given E_{rel}). Creep buckling at finite time occurs for pressures between the heavy curve and light curve. It is important to emphasize again that the imperfection sensitivity plots in Fig. 16 are essentially independent of both h/R and the base angle, α_0, if the shells are thin, deep and if β_I scales with $\sqrt{h/R}$.

5. Conclusions

This paper establishes a viscoelastic shell theory for predicting the nonlinear time-dependent buckling behavior of viscoelastic spherical shells subjected to uniform external pressure. The small-strain, moderate-rotation shell theory is used in conjunction with the standard linear solid to describe viscoelastic shells with geometric imperfections. The equilibrium equations are obtained by the principle of virtual work. Analyses are carried out numerically for two types of loadings representative of those employed in experimental studies, one involving volume control and the other pressure control. Specifically, under volume control a rate of volume change is prescribed, and under pressure control a pressure is prescribed that is applied very rapidly and then held constant.

Buckling behavior of spherical shells is investigated for these two classes of loadings over the full range of viscoelasticity and imperfection amplitude with emphasis on exposing the imperfection sensitivity as well as the time-dependence. An important and unexpected coincidence of the limits for short-time elastic buckling and long-time creep buckling is discovered and discussed in Section 4 for the constant pressure loadings. The coincidence can be stated simply as the following. For a given imperfection, the short-time elastic buckling limit, normalized as p/p_c, is equal to the long-time creep buckling limit, normalized as p/p_c^∞, where p_c is the elastic buckling pressure of the perfect shell determined using the short-time elastic modulus, $E_1 + E_\infty$, and p_c^∞ is the elastic buckling pressure of the perfect shell determined using the long-time elastic modulus, E_∞. The simplicity of this result permits construction of a map of buckling behavior over the entire range of pressure, imperfection amplitude and viscosity. The map delineates three regimes of

behavior: no buckling, creep buckling at finite time, and essentially instantaneous elastic buckling.

In this work, we focus on the buckling of viscoelastic shells under the assumption of axisymmetry. It should be noted that shells could undergo a secondary buckling transition, where the dimple loses its axisymmetry at sufficiently large volume changes (Knoche and Kierfeld, 2014), and the non-axisymmetric buckling has been studied in literature (Hutchinson, 2016; Knoche and Kierfeld, 2014; Taffetani et al., 2018). In those cases, non-axisymmetric shell equations with bifurcation analysis are needed.

Experiments would be good validations for the theoretical predictions in this work. The creep buckling phenomenon of spherical shells has been demonstrated in the existing literature (Stein-Montalvo et al., 2021), but systematic experiments are needed, which will be a topic for future work.

CRediT authorship contribution statement

Tianzhen Liu: Data curation, Formal analysis, Methodology, Software, Writing – original draft, Writing – review & editing. **Yuzhen Chen:** Formal analysis, Validation, Writing – review & editing. **John W. Hutchinson:** Conceptualization, Investigation, Methodology, Supervision, Writing – review & editing. **Lihua Jin:** Conceptualization, Formal analysis, Funding acquisition, Investigation, Methodology, Supervision, Writing – review & editing.

Declaration of Competing Interest

The authors declare no conflict of interest.

Data availability

Data will be made available on request.

Acknowledgements

This work is supported by the startup fund from Henry Samueli School of Engineering and Applied Science at the University of California, Los Angeles, and National Science Foundation through a CAREER Award No. CMMI-2048219. T. L. acknowledge the support by the Fundamental Research Funds for the Central Universities (No. 2242022R20022) and Jiangsu Funding Program for Excellent Postdoctoral Talent (No. 2022ZB133).

Appendix

Appendix A. Derivation of equilibrium equations using principle of virtual work

In Section 2.3, the equilibrium equations are derived by postulating the principle of virtual work. Here, the details of the derivation are presented. According to Eq. (11), the internal virtual work of the shell under axisymmetric deformation can be expressed as

$$IVW = \int_s (N_{\omega\omega}\delta E_{\omega\omega} + N_{\theta\theta}\delta E_{\theta\theta} + M_{\omega\omega}\delta K_{\omega\omega} + M_{\theta\theta}\delta K_{\theta\theta})dS. \tag{A.1}$$

Based on the middle surface strains and bending strains in Eq. (3), the virtual strain components are written as

$$\begin{aligned}
\delta E_{\omega\omega} &= \delta W - \left(\delta\varphi + \delta W_{,\theta}\right)\tan\theta,\\
\delta E_{\theta\theta} &= \delta W + \delta\varphi_{,\theta} + \delta W_{,\theta\theta} + \varphi\delta\varphi - W_{I,\theta}\delta\varphi,\\
\delta K_{\omega\omega} &= -\frac{1}{R}\delta\varphi\tan\theta,\\
\delta K_{\theta\theta} &= \frac{1}{R}\delta\varphi_{,\theta}.
\end{aligned} \tag{A.2}$$

Substituting Eq. (A.2) into Eq. (A.1), the internal virtual work is given in Eq. (A.3),

$$IVW = \int_s \left[N_{\omega\omega}\left(\delta W - \left(\delta\varphi + \delta W_{,\theta}\right)\tan\theta\right) + N_{\theta\theta}\left(\delta W + \delta\varphi_{,\theta} + \delta W_{,\theta\theta} + \varphi\delta\varphi - W_{I,\theta}\delta\varphi\right) - M_{\omega\omega}\frac{1}{R}\delta\varphi\tan\theta + M_{\theta\theta}\frac{1}{R}\delta\varphi_{,\theta}\right]dS. \tag{A.3}$$

Applying the divergence theorem to the derivative terms (twice to the second derivative term), we can obtain

$$
\begin{aligned}
IVW \quad = \quad & \int_s \left[N_{\omega\omega}(\delta W - \delta\varphi\tan\theta) + \left(N_{\omega\omega,\theta}\tan\theta + N_{\omega\omega}\frac{1}{\cos^2\theta} \right)\delta W + N_{\theta\theta}\left(\delta W + \varphi\delta\varphi - W_{I,\theta}\delta\varphi\right) - N_{\theta\theta,\theta}\delta\varphi \right. \\
& \left. + N_{\theta\theta,\theta\theta}\delta W - \frac{1}{R}M_{\omega\omega}\delta\varphi\tan\theta - \frac{1}{R}M_{\theta\theta,\theta}\delta\varphi \right] dS \\
& + \oint_c \left(- N_{\omega\omega}\tan\theta n_\theta \delta W + N_{\theta\theta}n_\theta\delta\varphi - N_{\theta\theta,\theta}n_\theta\delta W + N_{\theta\theta}n_\theta n_\theta \delta W_{,n} - \left(N_{\theta\theta}n_\theta t_\theta\right)_{,t}\delta W + \frac{1}{R}M_{\theta\theta}n_\theta\delta\varphi \right) ds \\
& + N_{\theta\theta}n_\theta t_\theta \delta W|_{corners}
\end{aligned}
\tag{A.4}
$$

where S denotes the area of the middle surface, C is the boundary, and n_θ and t_θ are the normal and tangent unit vectors on C.

When the shell is subjected to a uniform inward pressure p in the radius direction, the external virtual work is expressed as in Eq. (12). EVW can be expressed as Eq. (A.5) using the second equation in Eq. (4).

$$
EVW = \int_s pR\delta W dS + \oint_C \left[Q\delta W + T_\theta\delta\varphi + (T_\theta n_\theta - M_n)\delta W_{,n} + T_\theta \delta W_{,t} t_\theta \right] R ds. \tag{A.5}
$$

Now we enforce IVW=EVW for all admissible virtual displacements δW and $\delta\varphi$ in S, and get

$$
\begin{aligned}
& N_{\omega\omega} + \tan\theta N_{\omega\omega,\theta} + \frac{1}{\cos^2\theta}N_{\omega\omega} + N_{\theta\theta} + N_{\theta\theta,\theta\theta} = pR, \\
& -N_{\omega\omega}\tan\theta + N_{\theta\theta}\varphi - N_{\theta\theta}W_{I,\theta} - N_{\theta\theta,\theta} - \frac{1}{R}\tan\theta M_{\omega\omega} - \frac{1}{R}M_{\theta\theta,\theta} = 0.
\end{aligned}
\tag{A.6}
$$

The equations can be normalized using Eqs. (10) and (13). Then the second equation, after a derivative with respect to θ is taken on both sides, is inserted into the first equation, and finally the equilibrium equations in Eq. (14) are obtained. Similarly, by independently varying δW, $\delta\varphi$ and $\delta W_{,n}$ on the boundary C for non-zero terms, we can obtain the relations among the boundary forces, moment and internal stress quantities

$$
\begin{aligned}
& Q = -N_{\omega\omega}\tan\theta n_\theta - N_{\theta\theta,\theta}n_\theta, \\
& T_\theta = N_{\theta\theta}n_\theta + \frac{1}{R}M_{\theta\theta}n_\theta, \\
& T_\theta n_\theta - M_n = N_{\theta\theta}n_\theta n_\theta.
\end{aligned}
\tag{A.7}
$$

Either Q or W, T_θ or φ, and $T_\theta n_\theta - M_n$ or $W_{,n}$ should be specified on C. Specifically, we employ $W = W_{,\theta} = \varphi = 0$ at the base for the clamped boundary condition in this work, which ensures the boundary term in Eq. (A.4) is satisfied.

References

Audoly, B., Hutchinson, J.W., 2019. Localization in spherical shell buckling. J. Mech. Phys. Solids 136, 103720.
Bartlett, N.W., Tolley, M.T., Overvelde, J.T.B., Weaver, J.C., Mosadegh, B., Bertoldi, K., Whitesides, G.M., Wood, R.J., 2015. A 3D-printed, functionally graded soft robot powered by combustion. Science 349, 161–165.
Błachut, J., Magnucki, K., 2008. Strength, stability, and optimization of pressure vessels: review of selected problems. Appl. Mech. Rev. 61, 1517–1526.
Brinkmeyer, A., Santer, M., Pirrera, A., Weaver, P., 2012. Pseudo-bistable self-actuated domes for morphing applications. Int. J. Solids Struct. 49, 1077–1087.
Budiansky, B., 1974. Theory of buckling and post-buckling behavior of elastic structures. Adv. Appl. Mech. 14, 1–65.
Carlson, R.L., Sendelbeck, R.L., Hoff, N.J., 1967. Experimental studies of the buckling of complete spherical shells. Exp. Mech. 7, 281–288.
Che, K., Rouleau, M., Meaud, J., 2019. Temperature-tunable time-dependent snapping of viscoelastic metastructures with snap-through instabilities. Extrem. Mech. Lett. 32, 100528.
Chen, Y., Jin, L., 2020. Snapping-back buckling of wide hyperelastic columns. Extrem. Mech. Lett. 34, 100600.
Chen, Y., Liu, T., Jin, L., 2022. Spatiotemporally programmable surfaces via viscoelastic shell snapping. Adv. Intell. Syst. 4, 2100270.
Cheng, L., Tang, T., Yang, H., Hao, F., Wu, G., Lyu, F., Bu, Y., Zhao, Y., Zhao, Y., Liu, G., Cheng, X., Lu, J., 2021. The twisting of dome-like metamaterial from brittle to ductile. Adv. Sci. 8, 2002701.
Dong, Y., Pezzulla, M., Reis, P.M., 2020. Buckling of pressurized spherical shells containing a through-thickness defect. J. Mech. Phys. Solids 138, 103923.
Dykstra, D.M., Busink, J., Ennis, B., Coulais, C., 2019. Viscoelastic snapping metamaterials. J. Appl. Mech. 86, 111012.
Evkin, A.Y., Lykhachova, O.V., 2017. Energy barrier as a criterion for stability estimation of spherical shell under uniform external pressure. Int. J. Solids Struct. 118-119, 14–23.
Evkin, A.Y., Lykhachova, O.V., 2019. Design buckling pressure for thin spherical shells: development and validation. Int. J. Solids Struct. 156, 61–72.
Faber, J.A., Udani, J.P., Riley, K.S., Studart, A.R., Arrieta, A.F., 2020. Dome-patterned metamaterial sheets. Adv. Sci. 7, 2001955.
Gerasimidis, S., Virot, E., Hutchinson, J.W., Rubinstein, S.M., 2018. On establishing buckling knockdowns for imperfection-sensitive shell structures. J. Appl. Mech. 85, 091010.
Gorissen, B., Melancon, D., Vasios, N., Torbati, M., Bertoldi, K., 2020. Inflatable soft jumper inspired by shell snapping. Sci. Robot. 5, eabb1967.
Grigoliuk, E.I., Lipovtsev, Y.V., 1969. On the creep buckling of shells. Int. J. Solids Struct. 5, 155–173.
Hayman, B., 1981. Creep buckling-a general view of the phenomena. Creep in Structures. Springer, pp. 289–307.
Hewitt, J.S., Mazumdar, J., 1977. Buckling of viscoelastic plates. AIAA J. 15, 451–452.
Huang, N.C., 1963. Unsymmetrical buckling of shallow spherical shells. AIAA J. 1, 945. -945.
Huang, N.C., 1964. Unsymmetrical buckling of thin shallow spherical shells. J. Appl. Mech. 14 (1–2), 111–122.
Huang, N.C., 1965. Axisymmetrical creep buckling of clamped shallow spherical shells. J. Appl. Mech. 32, 323–330.
Huang, N.C., 1967. Nonlinear creep buckling of some simple structures. J. Appl. Mech. 34, 651–658.
Hutchinson, J.W., 2016. Buckling of spherical shells revisited. Proc. R. Soc. A Math. Phys. 472, 20160577.
Hutchinson, J.W., Koiter, W.T., 1970. Postbuckling theory. Appl. Mech. Rev. 23, 1353–1366.

Hutchinson, J.W., Thompson, J.M., 2017. Nonlinear buckling interaction for spherical shells subject to pressure and probing forces. J. Appl. Mech. 84, 061001.
Hutchinson, J.W., Thompson, J.M.T., 2018. Imperfections and energy barriers in shell buckling. Int. J. Solids Struct. 148–149, 157–168.
Janbaz, S., Narooei, K., Manen, T.V., Zadpoor, A.A., 2020. Strain rate–dependent mechanical metamaterials. Sci. Adv. 6, eaba0616.
Jones, N., 1976. Creep buckling of a complete spherical shell. J. Appl. Mech. 43, 450–454.
Jose, J., Kamp, M., van Blaaderen, A., Imhof, A., 2014. Unloading and reloading colloidal microcapsules with apolar solutions by controlled and reversible buckling. Langmuir 30, 2385–2393.
Kao, R., 1981. Nonlinear creep buckling analysis of initially imperfect shallow spherical shells. Comput. Struct. 14, 111–122.
Kaplan, A., Fung, Y.C., 1954. A Nonlinear Theory of Bending and Buckling of Thin Elastic Shallow Spherical Shells. National Advisory Committee for Aeronautics, Washington. DC Technical Note 3212.
Karman, V.T., Tsien, H., 1939. The buckling of spherical shells by external pressure. J. Aeronaut. Sci. 7, 43–50.
KEMPNER, J., 1954. Creep Bending and Buckling of Linearly Viscoelastic Columns. NASA. Technical Note 3136.
Kierzenka, J., Shampine, L.F., 2001. A BVP solver based on residual control and the Maltab PSE. ACM Trans. Math. Softw. (TOMS) 27 (3), 299–316.
Knoche, S., Kierfeld, J., 2014. The secondary buckling transition: wrinkling of buckled spherical shells. Eur. Phys. J. C Part Fields 37, 1–21.
Kochmann, D.M., Bertoldi, K., 2017. Exploiting microstructural instabilities in solids and structures: from metamaterials to structural transitions. Appl. Mech. Rev. 69, 050801.
Koga, T., Hoff, N.J., 1969. The axisymmetric buckling of initially imperfect complete spherical shells. Int. J. Solids Struct. 5, 679–697.
Koiter, W.T., 1966. On the nonlinear theory of thin elastic shells. Proc. K. Ned. Akad. Wet. B69, 1–54.
Koiter, W.T., 1969. The nonlinear buckling problem of a complete spherical shell under uniform external pressure. I-IV Proc. K. Ned. Akad. Wet. B72, 40–123.
Krenzke, M.A., Kiernan, T.J., 1963. Elastic stability of near-perfect shallow spherical shells. AIAA J. 1, 2855–2857.
Lakes, R.S., 1998. Viscoelastic Solids. CRC press.
Lee, A., López Jiménez, F., Marthelot, J., Hutchinson, J.W., Reis, P.M., 2016. The geometric role of precisely engineered imperfections on the critical buckling load of spherical elastic shells. J. Appl. Mech. 83, 111005.
Liu, T., Chen, Y., Liu, L., Liu, Y., Leng, J., Jin, L., 2021. Effect of imperfections on pseudo-bistability of viscoelastic domes. Extrem. Mech. Lett. 49, 101477.
Marques, S., Creus, G.J., 1994. Geometrically nonlinear finite element analysis of viscoelastic composite materials under mechanical and hygrothermal loads. Comput. Struct. 53, 449–456.
Minahen, T.M., Knauss, W.G., 1993. Creep buckling of viscoelastic structures. Int. J. Solids Struct. 30, 1075–1092.
Miyazaki, N., Hagihara, S., 2015. Creep buckling of shell structures. Mech. Eng. Rev. 2, 14–00522.
Miyazaki, N., Yagawa, G., Ando, Y., 1977. A parametric analysis of creep buckling of a shallow spherical shell by the finite element method. Nucl. Eng. Des. 41, 257–263.
Nachbar, W., Huang, N.C., 1967. Dynamic snap-through of a simple viscoelastic truss. Q. Appl. Math. 25, 65–82.
NASA, 1969. Buckling of Thin-Walled Doubly Curved Shells. NASA. NASA Space Veh. Des. Criteria NASA SP-8032.
Obrecht, H., 1977. Creep buckling and postbuckling of circular cylindrical shells under axial compression. Int. J. Solids Struct. 13, 337–355.
Paulose, J., Nelson, D.R., 2013. Buckling pathways in spherical shells with soft spots. Eur. Phys. J. E Soft Matter 9, 8227–8245.
Qiao, C., Liu, L., Pasini, D., 2020. Elastic thin shells with large axisymmetric imperfection: from bifurcation to snap-through buckling. J. Mech. Phys. Solids 141, 103959.
Qiao, C., Liu, L., Pasini, D., 2021. Bi-shell valve for fast actuation of soft pneumatic actuators via shell snapping interaction. Adv. Sci. 8, 2100445.
Reis, P.M., 2015. A perspective on the revival of structural (in) stability with novel opportunities for function: from buckliphobia to buckliphilia. J. Appl. Mech. 82, 111001.
Sanders, J.L., 1963. Nonlinear theories for thin shells. Q. Appl. Math. 21, 21–36.
Stein-Montalvo, L., Holmes, D.P., Coupier, G., 2021. Delayed buckling of spherical shells due to viscoelastic knockdown of the critical load. Proc. R. Soc. A 447, 20210253.
Taffetani, M., Jiang, X., Holmes, D.P., Vella, D., 2018. Static bistability of spherical caps. Proc. R. Soc. A Math. Phys. Eng. Sci. 474, 20170910.
Vasios, N., Deng, B., Gorissen, B., Bertoldi, K., 2021. Universally bistable shells with nonzero Gaussian curvature for two-way transition waves. Nat. Commun. 12, 695.
Vinogradov, A.M., 1987. Buckling of viscoelastic beam columns. AIAA J. 25, 479–483.
Vinogradov, A.M., Glockner, P.G., 1980. Buckling of spherical viscoelastic shells. J. Struct. Div. Am. Soc. Civ. Eng. 106, 59–67.
Wilson, D.W., Vinson, J.R., 1984. Viscoelastic analysis of laminated plate buckling. AIAA J. 22, 982–988.
Xirouchakis, P.C., Jones, N., 1980. Axisymmetric and bifurcation creep buckling of externally pressurised spherical shells. Int. J. Solids Struct. 16, 131–148.
Yang, Y., Vella, K., Holmes, D.P., 2021. Grasping with kirigami shells. Sci. Robot. 6, eabd6426.
Zoelly, R., 1915. Ueber ein Knickungsproblem an der Kugelschale. ETH Zürich, Zürich, Switzerland. Zürich.